

# JGR Space Physics

## RESEARCH ARTICLE

10.1029/2020JA027908

### Key Points:

- We developed the first deep learning model to predict the dynamics of AMPERE-derived field aligned currents
- When IMF changes abruptly, the initial response and total reconfiguration time of FACs vary with MLT and season
- For an abrupt change in IMF Bz or By, our model predicts an exponential response in FACs

### Correspondence to:

B. S. R. Kunduri,  
bharatr@vt.edu

### Citation:

Kunduri, B. S. R., Maimaiti, M., Baker, J. B. H., Ruohoniemi, J. M., Anderson, B. J., & Vines, S. K. (2020). A deep learning-based approach for modeling the dynamics of AMPERE Birkeland currents. *Journal of Geophysical Research: Space Physics*, 125, e2020JA027908. <https://doi.org/10.1029/2020JA027908>

Received 11 FEB 2020

Accepted 13 JUL 2020

Accepted article online 29 JUL 2020

## A Deep Learning-Based Approach for Modeling the Dynamics of AMPERE Birkeland Currents

B. S. R. Kunduri<sup>1</sup> , M. Maimaiti<sup>1</sup> , J. B. H. Baker<sup>1</sup> , J. M. Ruohoniemi<sup>1</sup> ,  
B. J. Anderson<sup>2</sup> , and S. K. Vines<sup>2</sup> 

<sup>1</sup>Bradley Department of Electrical and Computer Engineering, Virginia Tech, Blacksburg, VA, USA, <sup>2</sup>The Johns Hopkins University Applied Physics Laboratory, Laurel, MD, USA

**Abstract** The existence of Birkeland magnetic field-aligned current (FAC) system was proposed more than a century ago, and it has been of immense interest for investigating the nature of solar wind-magnetosphere-ionosphere coupling ever since. In this paper, we present the first application of deep learning architecture for modeling the Birkeland currents using data from the Active Magnetosphere and Planetary Electrodynamics Response Experiment (AMPERE). The model uses a 1-hr time history of several different parameters such as interplanetary magnetic field (IMF), solar wind, and geomagnetic and solar indices as inputs to determine the global distribution of Birkeland currents in the Northern Hemisphere. We present a comparison between our model and bin-averaged statistical patterns under steady IMF conditions and also when the IMF is variable. Our deep learning model shows good agreement with the bin-averaged patterns, capturing several prominent large-scale features such as the Regions 1 and 2 FACs, the NBZ current system, and the cusp currents along with their seasonal variations. However, when IMF and solar wind conditions are not stable, our model provides a more accurate view of the time-dependent evolution of Birkeland currents. The reconfiguration of the FACs following an abrupt change in IMF orientation can be traced in its details. The magnitude of FACs is found to evolve with e-folding times that vary with season and MLT. When IMF Bz turns southward after a prolonged northward orientation, NBZ currents decay exponentially with an e-folding time of ~25 min, whereas Region 1 currents grow with an e-folding time of 6–20 min depending on the MLT.

## 1. Introduction

The existence of a field-aligned current (FAC) system was first proposed by Kristian Birkeland (Birkeland, 1908) and later confirmed by Zmuda et al. (1966). Since then, data from magnetometers on several satellite missions such as Dynamics Explorer 2 (Weimer, 2001), Orsted/Magsat (Papitashvili et al., 2002), DMSP (Ohtani et al., 2005), and Challenging Minisatellite Payload (CHAMP) (Laundal, Finlay, et al., 2018; Laundal, Reistad, et al., 2018) have provided crucial insights into the nature of solar wind-magnetosphere-ionosphere coupling (e.g., Iijima & Potemra, 1976a; Lysak, 1990; Milan et al., 2018). For example, the large-scale structure and magnitude of FACs are strongly controlled by the interplanetary magnetic field (IMF) and season (e.g., Fujii et al., 1981; Iijima & Potemra, 1976a, 1978; Potemra, 1985). Depending on the orientation and magnitude of IMF Bz and By, three major current systems were reported: (1) the Region 1 and Region 2 currents (e.g., Anderson et al., 2008; Iijima & Potemra, 1976a, 1978; Weimer, 2001), (2) Region 0 or cusp currents (e.g., Erlandson et al., 1988; Iijima & Potemra, 1976b; Saunders, 1989), and (3) NBZ currents (e.g., Iijima et al., 1984; Iijima & Shibaji, 1987; Mauk & Zanetti, 1987; Saunders, 1989). On average, currents were found to be stronger in the summer hemisphere (e.g., Fujii et al., 1981; Laundal et al., 2016), in some cases by a factor of 2–3 (Ohtani et al., 2005). The impact of season was particularly strong on the dayside current system and was noted to significantly reduce the intensity of the NBZ and cusp currents during winter (e.g., Green et al., 2009; Papitashvili et al., 2002; Weimer, 2001). Due to the restricted spatio-temporal coverage of the earlier missions, most of our understanding pertaining to the Birkeland currents was limited to static and steady-state conditions. However, during the last solar cycle, the Active Magnetosphere and Planetary Electrodynamics Response Experiment (AMPERE) project started providing global maps of the Birkeland current system at a 10-min cadence (Anderson et al., 2000, 2002; Waters et al., 2001), opening up new possibilities to explore their dynamics (Coxon et al., 2018; Matsuo et al., 2015; Murphy et al., 2012).

**Table 1**  
Mean and Standard Deviation in the Input Parameters (Between 1 January 2010 and 1 January 2016) Used for Normalizing the Data

Input parameters	Mean	Standard deviation
Bz (nT)	0.00193	3.392
By (nT)	−0.008	3.928
Bx (nT)	0.084	3.366
Vx (km/s)	−409.66	89.08
Np (cm <sup>−3</sup> )	5.90	4.80
AU (nT)	238.28	1,493.80
AL (nT)	−234.71	1,099.24
Sym-H (nT)	−10.52	16.68
Asym-H (nT)	19.06	13.88
F10.7 (sfu)	116.59	27.94

Note. See section 2.1 for details.

Statistical characterizations of the Birkeland current system presented in previous studies are in good overall agreement for stable IMF conditions (for e.g., Green et al., 2009; Iijima & Potemra, 1976a; Weimer, 2001). However, there have been conflicting results pertaining to the response of the high-latitude ionosphere to a change in the IMF (Anderson et al., 2018; Lockwood et al., 1986; Ridley et al., 1998; Ruohoniemi et al., 2002; Saunders et al., 1992). In particular, a key question has generated a lot of debate in the community, namely: Is the onset of the ionospheric response to abrupt changes in IMF simultaneous across all magnetic local time (MLT) sectors? Early studies with the EISCAT radar (Lockwood et al., 1986) and magnetometers (Saunders et al., 1992) suggested the response of ionospheric convection to southward turning of IMF propagates away from noon, resulting in a time delay on the order of a few tens of minutes near dusk (Saunders et al., 1992). Later, contradictory results were presented by Ridley et al. (1997, 1998), who used the Assimilative Mapping of Ionospheric Electrodynamics (AMIE) procedure (Richmond, 1992) and showed the response to a southward turning of IMF is globally simultaneous (within a few minutes). This global response was further demonstrated by Ruohoniemi and Greenwald (1998) using observations from Super Dual Auroral Radar Network (SuperDARN). More recently, Snekvik et al. (2017) analyzed magnetic field perturbations from the AMPERE project during periods of dayside reconnection and showed that the initial response is almost simultaneous across all MLT sectors. They further reported that the initial response is strongest near noon, whereas the response on the nightside grew stronger after an initial delay of ~10 min. Clearly, the response of high-latitude ionosphere to changes in IMF is still an active area of research, and several key aspects such as the reconfiguration times (Milan et al., 2018; Moretto et al., 2018) associated with the Birkeland currents are yet to be determined.

Statistical and empirical models of the Birkeland currents have generally been limited to steady-state IMF conditions (Green et al., 2009; Papitashvili et al., 2002; Weimer, 2001). Developing a “data-based” model to predict these currents when the IMF and solar wind are variable has been particularly challenging because of (1) the limitations in spatio-temporal coverage provided by earlier missions (such as Dynamics Explorer 2 and DMSP) and (2) limitations of traditional time series prediction tools such as Autoregressive Integrated Moving Average (ARIMA) (Siami-Namini & Namin, 2018; Wang et al., 2017). However, recent studies have demonstrated that deep learning can be a very powerful tool that can be used to model time series data such as wind speed (Chen et al., 2018) and the stock market (Qin et al., 2017), even when the data set is noisy (Zhang et al., 2016). These studies show that deep learning architectures have great potential to model the dynamics of spatio-temporal phenomena such as the Birkeland currents.

In this study, we take advantage of the recent advancements in deep learning to model the time-dependent evolution of AMPERE FACs in the Northern Hemisphere. The large and continuously available database of global Birkeland current patterns provided by the AMPERE project is ideally suitable for training deep learning architectures that are capable of capturing such complicated behavior (LeCun et al., 2015; Maimaiti et al., 2019). To this end, we use a 60-min time history of solar wind bulk speed (Vx), proton number density (Np), IMF components (Bx, By, and Bz), and geomagnetic and solar indices (Sym-H, Asym-H, SuperMAG AL/AU, and F10.7 flux) along with the month (indicative of season) as inputs to a convolutional neural network (CNN) model to estimate global Birkeland currents at a given moment.

Statistical and empirical models of the Birkeland currents have generally been limited to steady-state IMF conditions (Green et al., 2009; Papitashvili et al., 2002; Weimer, 2001). Developing a “data-based” model to predict these currents when the IMF and solar wind are variable has been particularly challenging because of (1) the limitations in spatio-temporal coverage provided by earlier missions (such as Dynamics Explorer 2 and DMSP) and (2) limitations of traditional time series prediction tools such as Autoregressive Integrated Moving Average (ARIMA) (Siami-Namini & Namin, 2018; Wang et al., 2017). However, recent studies have demonstrated that deep learning can be a very powerful tool that can be used to model time series data such as wind speed (Chen et al., 2018) and the stock market (Qin et al., 2017), even when the data set is noisy (Zhang et al., 2016). These studies show that deep learning architectures have great potential to model the dynamics of spatio-temporal phenomena such as the Birkeland currents.

In this study, we take advantage of the recent advancements in deep learning to model the time-dependent evolution of AMPERE FACs in the Northern Hemisphere. The large and continuously available database of global Birkeland current patterns provided by the AMPERE project is ideally suitable for training deep learning architectures that are capable of capturing such complicated behavior (LeCun et al., 2015; Maimaiti et al., 2019). To this end, we use a 60-min time history of solar wind bulk speed (Vx), proton number density (Np), IMF components (Bx, By, and Bz), and geomagnetic and solar indices (Sym-H, Asym-H, SuperMAG AL/AU, and F10.7 flux) along with the month (indicative of season) as inputs to a convolutional neural network (CNN) model to estimate global Birkeland currents at a given moment.

One set of crucial inputs to our model are the IMF components (Bz, By, and Bx) and solar wind X-component speed and number density (Vx and Np) parameters. In the current study, we use 1-min averaged OMNI values (King & Papitashvili, 2005), time shifted to the bow shock. A uniform 10-min delay was added to the OMNI solar wind and IMF data to account for the propagation time of the solar wind through the magnetosheath and the time for AMPERE to express the influence of the solar wind on the FACs (Wing et al., 2002). Finally, we normalized these values by subtracting the mean and divide by standard

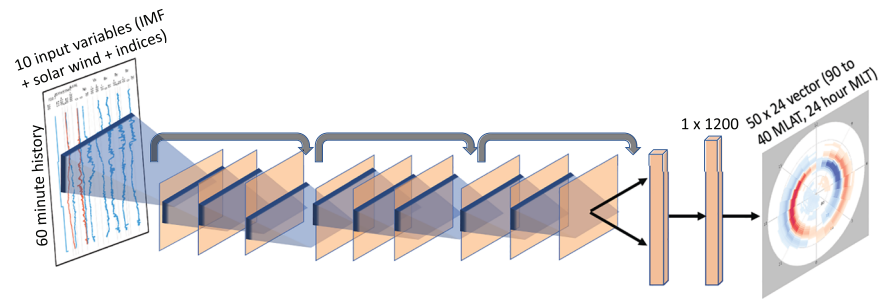


**Figure 1.** An illustration of the CNN architecture with three ResNet units. The input layer takes a 2-D input array with 60 (minutes history)  $\times$  11 (parameters indicating solar and geomagnetic activity and season) dimensions, and the output layer produces estimated AMPERE currents in the Northern Hemisphere. Each polyhedron between the adjacent convolution layers represents the mapping of a previous layer to the next through a 2-D convolution. The three curved downward pointing arrows indicate the ResNet units.

deviation (a standard practice in machine learning to improve the performance of the backpropagation algorithm). The mean and standard deviation of the input parameters are listed in Table 1.

To incorporate the impact of geomagnetic disturbances at midlatitudes, the longitudinally asymmetric (Asym-H) and symmetric (Sym-H) disturbance indices (Iyemori, 1990) were used as inputs to our model. The Sym-H and Asym-H indices have a higher temporal resolution of 1 min compared to the 1-hr resolution of the Dst index and are thus more suitable for the current study. These indices were accessed through the Geomagnetic Data Service, Kyoto, Japan. The impact of auroral electrojets was incorporated using SuperMAG derived AL and AU indices (Gjerloev, 2012), and the 10.7-cm solar radio flux (F10.7) was used as a proxy for solar activity (Tapping, 2013). Finally, to model the influence of season, we used month as an input feature to the model. Since season is a cyclical feature, we transformed month into two new input parameters using a sine and cosine transformation to accurately represent its impact.

## 2.2. AMPERE FACs

The AMPERE project provides global maps of the Birkeland current system using measurements of magnetic field perturbations from the magnetometers on board the Iridium satellite constellation (Anderson et al., 2000, 2002; Waters et al., 2001). The Iridium constellation consists of 66+ commercial satellites in 780-km polar circular orbits, distributed over six equally spaced orbital planes, with 2-hr local time separation. Each satellite carries an engineering-grade magnetometer. Perturbations measured by these magnetometers are processed to remove the background International Geomagnetic Reference Field (IGRF) and long-period residuals from the observations, following which a spherical harmonic inversion technique is used to derive the FACs in the polar regions (Anderson et al., 2000; Waters et al., 2001). These global FAC maps are provided at a 10-min cadence on a spatial grid spanning 1 hr in MLT and  $1^\circ$  in magnetic latitude (MLAT). The AMPERE project has provided estimates of FACs over both hemispheres nearly continuously since 2010, making the data set ideally suited for training deep learning applications. In this study, we train the model on data between 1 January 2010 and 1 January 2016.

## 2.3. CNN Model

Our goal in this study is to model the evolution of FACs based on a time history of IMF. In particular, we aim to capture two features as accurately as possible: (1) the reconfiguration of the FAC system from one steady state to another and (2) the response of FACs to a change in IMF at different locations. Both these tasks require a model that is suitable for capturing complex features in a temporal data set, and a ResNet CNN is one such model (Fawaz et al., 2019; He, Zhang, et al., 2016; Maimaiti et al., 2019). Furthermore, the ResNet CNN architecture is less prone to the adverse effects associated with deeper architectures and is relatively easier to optimize (Glorot & Bengio, 2010). Deep learning models require a lot of data, and they tend to work best when the data are continuous in both space and time (e.g., Lake et al., 2015, 2017). This aspect makes the AMPERE project (Anderson et al., 2000, 2002), which has been providing global FAC maps continuously with a temporal resolution of 10 min over the last several years, ideally suitable for training such models. For these reasons, we decided to adopt a ResNet CNN architecture to model FACs using time

histories of IMF, solar wind, and geomagnetic indices as inputs. Hereafter, we will refer to this model as the CNN model.

In Figure 1, we present a schematic of our CNN model architecture. The input layer is a 2-D array with 60 (minute time history)  $\times$  11 (solar wind, IMF, geomagnetic indices, and F10.7 flux) dimensions. Specifically, we use Vx, Np, Bz, By, Bx, Sym-H, Asym-H, AL, AU, and F10.7 flux alongside sine and cosine transform of the month (see section 2.1) as inputs. The input layer is followed by three ResNet units, each made up of three identical convolution layers stacked in series. A “shortcut” connection between the input and output of each ResNet unit performs an identity mapping, and its output is added to the output of the next stack of convolution layers. The primary advantage of a ResNet unit is that it helps overcome the problem of vanishing/exploding gradients that are often encountered in deep architectures (He, Zhang, et al., 2016). When training such deep models, repeated multiplication can cause the backpropagated gradients to grow very large (or small), thereby causing the vanishing/exploding gradients problem. As a result, the gradient descent update leaves the weights from the initial layers virtually unchanged, and the training never converges to a good solution; a ResNet unit can help mitigate the problem. The output from the final ResNet unit is transformed to form a flattened 1-D layer, which is further transformed to another 1-D ( $1 \times 1,200$  units) layer. Finally, the last layer having  $1 \times 1,200$  dimensions is transformed into a 2-D map of predicted AMPERE FACs, with  $50 \times 24$  dimensions (providing FAC estimates between 40 and 90 MLAT at  $1^\circ$  resolution and 24 hr in MLT with 1-hr resolution). We trained several variations of the CNN model to optimize hyperparameters such as the number of ResNet units, and the model presented in Figure 1 was selected as optimal based on the mean absolute error.

Our CNN model is implemented in Keras with a Tensorflow backend (Chollet, 2015) and trained on the GPU infrastructure provided by Virginia Tech's Advanced Research Computing. As with any deep learning approach, the objective of our model was to minimize a loss function by optimizing the network's weights according to a backpropagation algorithm (Rumelhart et al., 1986). For our specific problem, the requirement was to use a loss function that can quantify the difference between predicted FACs and actual AMPERE observations on a global scale. We tested several different loss functions such as root mean squared error, mean absolute error, and correlation coefficient loss and found that the choice of loss function had no significant impact on the training process. We therefore chose the mean absolute error as the most intuitively obvious loss function. We used the “Adam” optimizer (Kingma & Ba, 2014) for stochastic gradient descent optimization. The adjustable parameters of “Adam” used in this study are learning rate  $\alpha = 0.002$ , learning rate decay = 0.0, and exponential decay rates  $\beta_1 = 0.9$  and  $\beta_2 = 0.999$  (see Kingma & Ba, 2014 for the definitions of these adjustable parameters). We trained our model using data between 1 January 2010 and 1 January 2016. A data point was constructed every 10 min and consisted of a Northern Hemisphere AMPERE FAC map and the corresponding 60-min history of the input parameters (see Figure 1 and section 2.1). We discarded unreliable data points when any of the input parameters were missing for more than 10 min continuously. Finally, we split the data set into three parts: train (90%), validation (9%), and test (1%) in chronological order, similar to the approach taken in Maimaiti et al. (2019). Such a split prevents the model from overfitting as the test and validation time periods are completely independent of the training time period. Moreover, all the data corresponding to the entire day as well as the previous and next days during an event (14 May 2013) analyzed in this study were manually removed from the training data set to make the analysis results completely independent of the training data set.

The choice of input parameters and their corresponding time history is another important “tunable” aspect of our model. We examined several models trained on different combinations of input parameters as well as input time history before choosing one with optimal performance (quantified by mean absolute error for the training and validation data sets). A summary of these models with different input combinations is presented in Table 2. Each row in the table represents a combination of IMF or geomagnetic/solar indices used as inputs and each column represents the length of their time history. The values in each cell show the corresponding mean absolute error ( $\mu\text{A}/\text{m}^2$ ) for the training/validation data sets. We chose the input parameters based on prior knowledge (e.g., Gjerloev, 2012; Iyemori, 1990; Laundal et al., 2016; Laundal, Finlay, et al., 2018; Weimer et al., 2003) of their role in influencing FACs as well as their availability over extended periods of time. However, we didn't use composite solar wind-magnetosphere coupling functions such as  $d\Phi/dt$  (Newell et al., 2007) as inputs to our model since previous studies have shown that deep



**Table 2**  
Model Performance for Different Input Parameters and Time History

	20 min	40 min	60 min	80 min
<b>IMF/SW + SMU/SML + SYM/ASY + F10.7</b>	<b>0.0735/0.0897</b>	<b>0.0733/0.0898</b>	<b>0.0731/0.0891</b>	<b>0.0732/0.0894</b>
IMF/SW + SMU/SML + SYM/ASY	0.0736/0.0908	0.0734/0.0903	<b>0.0733/0.0895</b>	0.0733/0.0895
IMF/SW + SMU/SML	0.0744/0.0926	0.0741/0.0907	<b>0.0739/0.0906</b>	0.0739/0.0905
IMF/SW only	0.0757/0.0937	0.0750/0.0917	<b>0.0747/0.0902</b>	0.0748/0.0903

Note. Each row represents different combinations of input parameters, and each column corresponds to a time history of the input parameters used during the training process. The values in each cell represent mean absolute errors ( $\mu\text{A}/\text{m}^2$ ) for training and validation data sets.

learning models can replicate the behavior of such functions and their addition doesn't substantially improve the model's performance any further (e.g., Maimaiti et al., 2019).

We trained the model on four different combinations of time history: 20, 40, 60, and 80 min. The first row of the table shows the mean absolute errors when all the input parameters (IMF and solar wind, SML/SMU, SYM/ASY, and F10.7 indices) are used for training the model. The second, third, and fourth rows show the mean absolute errors of models trained with consecutively lesser number of input parameters. For example, in the second row, the F10.7 index is not used as an input, and in the third row, both F10.7 and SYM/ASY indices are discarded. Removing the geomagnetic indices one at a time gradually reduces the model performance, and as expected, the model with the highest errors is the one trained only on IMF and solar wind parameters. We tested several different combinations of input parameters and are only summarizing the best four-, three-, two-, and one-parameter models in the table. The rows and columns with lowest errors are highlighted. Note that the training and validation errors systematically decrease as time history increases up until 60 min, beyond which there is no significant change in the error. Based on the mean absolute errors listed in Table 2, we selected the model with 60-min time history and all the input parameters (IMF and solar wind, SML/SMU, SYM/ASY, and F10.7 indices) included for further analysis. It is not surprising that our deep learning model with several geomagnetic and solar indices alongside IMF and solar wind parameters as inputs provides a much more accurate view of the FACs as compared to a model which is trained only on IMF and solar wind data. However, such a model has limited utility as a space weather forecasting tool since several geomagnetic and solar indices are not available in real-time unlike solar wind and IMF data from upstream satellites. We therefore suggest two possible approaches to increase our model's utility as a forecasting tool: (1) predicted values of geomagnetic and solar indices (Liemohn et al., 2018 and references therein) can be used as inputs to our model and (2) use the version of our model trained only on IMF and solar wind as input for forecasting purposes. In that regard, we have open-sourced all our code and both the models on Github for community use (see acknowledgements section).

#### 2.4. Bin-Averaged Statistical Model

To validate our CNN model under steady-state conditions and to further demonstrate its utility during intervals of variable IMF, we first compare its predictions with bin-averaged statistical patterns in the next sections. The bin-averaged statistical patterns were created using the exact same data set used for developing the CNN model. This means any differences can be wholly attributed to methodology, rather than to the underlying data. Specifically, we used the time stamps from the time-delayed OMNI data set (see section 2.1) to bin the 10-min cadence AMPERE data and derive average current density at IMF magnitudes ranging from 5 through 15 nT for eight equally spaced IMF clock angles (0 through 360) with a  $45^\circ$  separation. Similar to the approach taken by Carter et al. (2016), all current densities with a magnitude less than  $0.1 \mu\text{A}/\text{m}^2$  were discarded from the analysis. To limit our analysis to stable IMF conditions, we only used intervals when IMF was stable for at least 20 min, both in terms of magnitude and clock angle. The 20-min stability condition used in our study is consistent with previous studies which have used intervals ranging between 10 and 35-min (e.g., Pettigrew et al., 2010; Ruohoniemi & Greenwald, 1996; Weimer, 2001). Finally, to account for seasonal variability, these time intervals were further subdivided based on the month May–August (summer), November–February (winter), and March–April and September–October (equinox). From hereon, we will refer to these average patterns as the “statistical model” for the remainder of this study.

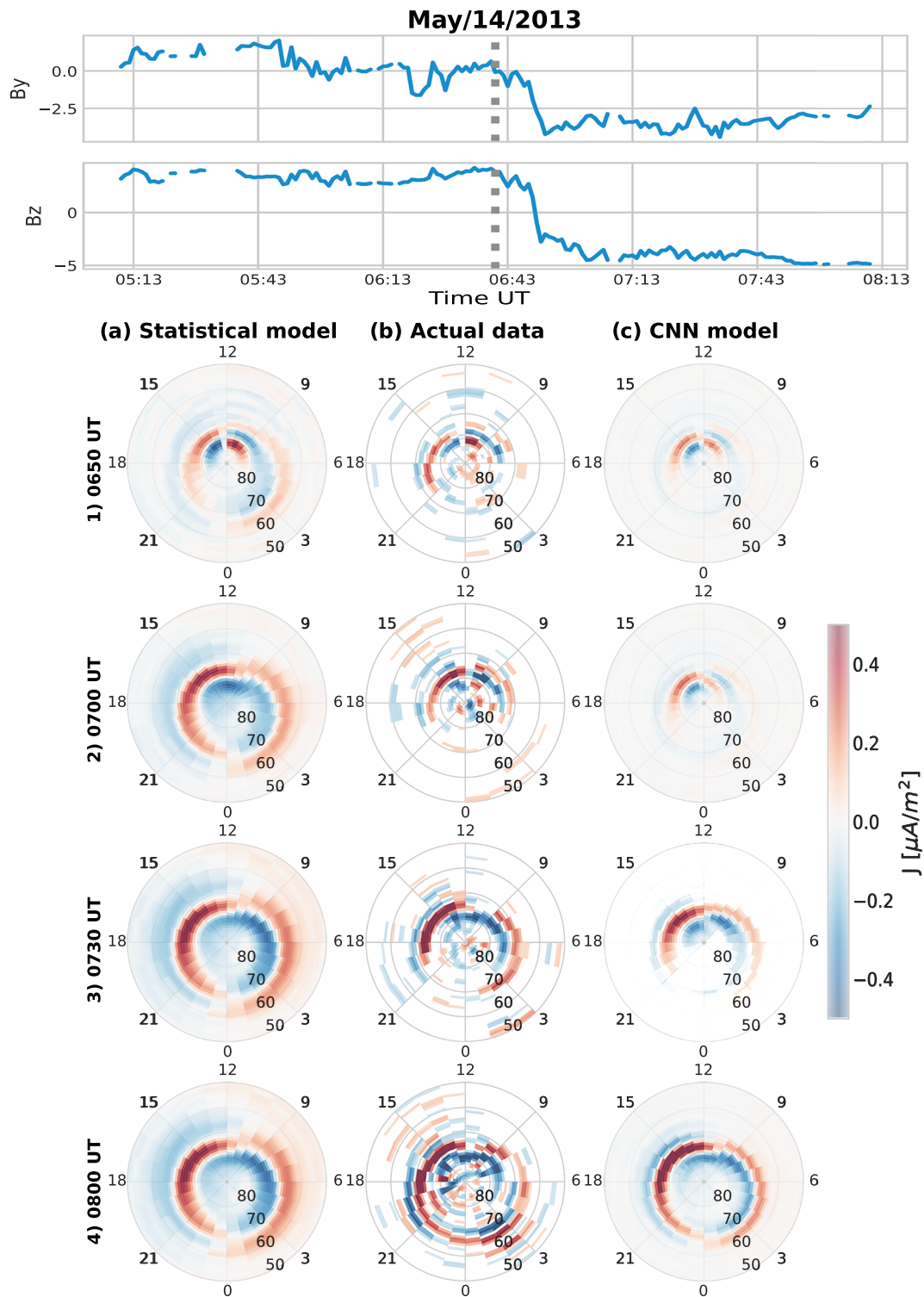


**Figure 2.** A sample prediction by the CNN model and a statistical model during an event on 14 May 2013. The first two panels show IMF By and Bz between 0500 and 0815 UT, and dashed lines mark the time period close to a shift in IMF orientation. The bottom four panels show a comparison between FAC current densities (a) estimated using the statistical model, (b) determined by AMPERE, and (c) predicted by the CNN model, at selected intervals during the event. See text for details.

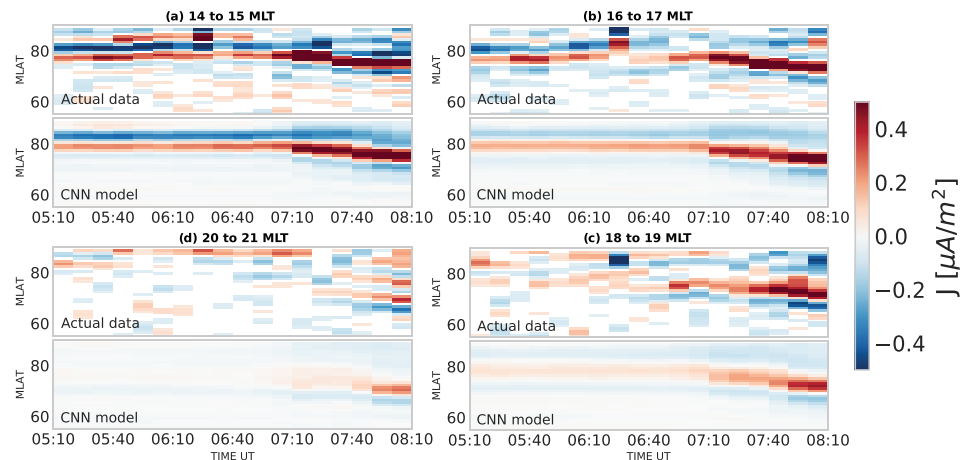


**Figure 3.** Latitude versus time plot depicting variations in current densities at different MLTs (a–d) for the event (14 May 2013) shown in Figure 2. Each panel presents a comparison between the median current densities determined by AMPERE (top subplot) and predicted by the CNN model (bottom subplot). The corresponding MLT sectors are indicated on top of each panel, and the current densities are color coded according to the color bar on the right.

### 3. Observations

In the previous sections, we focused on the data sets, model architecture, and training. In particular, we discussed the utility of a ResNet CNN architecture in modeling complex temporal features associated with the Birkeland current system. In this section, we present the CNN model predictions under widely varying solar and geomagnetic conditions, validate them against the statistical model, and finally analyze the response of the Birkeland current system to sudden changes in IMF.

#### 3.1. Case Study Analysis : 0510 to 0810 UT on 14 May 2013

Figure 2 shows a prediction made by our CNN model at 0510–0810 UT on 14 May 2013 compared with actual AMPERE observations as well as the statistical model. The top two panels show IMF  $B_y$  and  $B_z$ , and the dotted vertical line marks a time instance ( $\sim 06:40$  UT) just prior to a sudden change in IMF during which IMF  $B_y$  dropped from a nearly zero value to lower than  $-2.5$  nT, whereas  $B_z$  turned from northward to southward. The bottom four panels show the statistical model estimates (left), actual data from AMPERE (center), and the CNN model predictions (right) at selected instances during the event. During the first time instance at 0650 UT (just before the transition in IMF), the statistical model estimates are based on the average IMF  $B_z$  and  $B_y$  values between 0630 and 0650 UT, which correspond to a magnitude of 5 nT and a clock angle of  $0^\circ$  (dominant  $B_z$  positive conditions). On the other hand, the CNN model predictions are based on the 60 min of IMF, solar wind, and geomagnetic indices between 0550 and 0650 UT. The second time instance presents a comparison at 0700 UT, immediately after the transition when the average IMF magnitude (over previous 20 min) remains at 5 nT, but the clock angle changes to  $270^\circ$  (dominant  $B_y$  negative conditions). Similarly, the statistical model estimates at 0730 and 0800 UT correspond to an IMF magnitude of 5 nT and a clock angle of  $225^\circ$ . It is evident that, unlike the statistical model estimates, FACs from actual AMPERE data do not reconfigure instantaneously. Instead, they are in good agreement with the CNN model, which shows that they slowly reconfigure over several minutes. For example, in Figure 2, we can note that immediately after the  $B_z$  southward turning (by 0700 UT), the statistical model shows a fully formed Region 1 and Region 2 FAC system along with the downward directed cusp currents in the postnoon sector. However, the actual AMPERE data and the CNN model show a different behavior, wherein the Region 1 and Region 2 FACs initially start developing on the dayside, and it takes an hour (0800 UT) for the Region 1/2 system and the cusp current system to fully develop. The statistical model by design can only show a transition as occurring between discrete states, which is unrealistic when the IMF changes abruptly. We believe our CNN model can be particularly useful in such a scenario.

In Figure 3, we present latitude versus time plots of median FAC densities (median values of FACs at the selected MLTs at every MLAT) at four different MLT sectors to further analyze the time-dependent

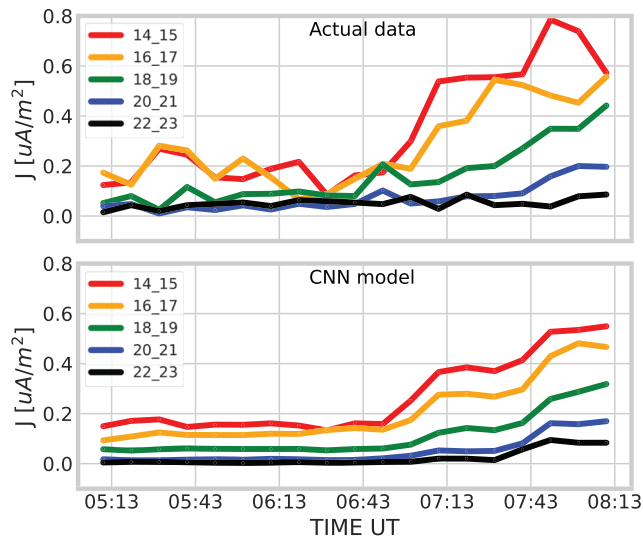


**Figure 4.** The time history of mean upward FAC densities determined by AMPERE (top panel) and predicted by the CNN model (bottom panel) for the event (14 May 2013) shown in Figure 2.

evolution of FACs on both the dayside and the nightside. Each subplot shows the actual data (top) and the CNN model (bottom) for the same event on 14 May 2013 presented in Figure 2. We note that the CNN model shows an increase in FAC densities (after a change in IMF orientation  $\sim 07:00$  UT) to values exceeding  $0.5 \mu\text{A}/\text{m}^2$  on the dayside (between 14 and 17 MLTs), in good agreement with the actual data. On the nightside, the upward Region 1 currents in actual AMPERE data are very weak ( $<0.2 \mu\text{A}/\text{m}^2$ ) and are centered at  $\sim 70$  MLAT, with a latitudinal width not exceeding  $2\text{--}3^\circ$ . In comparison, the CNN model is in good agreement with the actual data both in terms of location and latitudinal width, albeit slightly underestimating the current densities. We further note two other important features from the figure. First, the CNN model predicts that the FACs gradually move to lower latitudes, in good agreement with actual data. Second, the CNN model and actual data indicate that the magnitude of response is much stronger on the dayside.

The similarities and differences between the AMPERE data (top) and the CNN model (bottom) are further evident in Figure 4, which shows the time history of mean upward Region 1 currents for the same event on 14 May 2013. Prior to the abrupt change in IMF orientation ( $\sim 0700$  UT), there isn't a lot of variability in the FACs and the

CNN model estimates FACs ranging between  $\sim 0$  and  $0.2 \mu\text{A}/\text{m}^2$ , in good agreement with AMPERE data. After the abrupt change in IMF, the CNN model predicts a gradual increase in the currents for  $\sim 40\text{--}50$  min and higher FAC densities on the dayside with peak values exceeding  $0.5 \mu\text{A}/\text{m}^2$ . Actual AMPERE observations show that the currents indeed take about  $40\text{--}50$  min to reach peak values varying between  $0.1$  and  $0.6 \mu\text{A}/\text{m}^2$ , in good agreement with the CNN model estimates. In later sections, we will further analyze the response of FACs to a change in IMF and its dependence on MLT and season.

### 3.2. Steady-State Analysis : Statistical Model Versus CNN Model

Before further analyzing our CNN model's response to variable IMF and solar wind conditions, it is necessary to validate its performance during steady-state conditions and determine if it is consistent with expectations based on standard statistical techniques. To that end, Figure 5 presents a comparison between our CNN model and the statistical model for four different clock angles during both summer and winter. The current patterns correspond to an IMF magnitude of  $5 \text{ nT}$  and represent (from top to bottom) dominant  $B_z$  positive,  $B_z$  negative,  $B_y$  positive, and  $B_y$  negative conditions, respectively. To calculate these steady-state patterns using the CNN model, we assume the corresponding IMF  $B_z$  and  $B_y$  values remain constant over the 60-min input history and the remaining parameters such as  $V_x$ ,  $N_p$ , and geomagnetic indices are substituted with average values (see Table 1). For example, to simulate steady-state  $B_z$  positive conditions (top panels), we manually input  $B_z = 5 \text{ nT}$  and  $B_y = 0 \text{ nT}$  (corresponding to a clock angle of  $0^\circ$ ) over the 60-min input period.

From Figure 5, we can clearly see that both the CNN and statistical models show a prominent Region 1/Region 2 current system (Iijima & Potemra, 1976a) with current densities exceeding  $0.6 \mu\text{A}/\text{m}^2$  during southward  $B_z$  conditions. When  $B_z$  is predominantly positive, both models show a strong NBZ current system (Potemra, 1985) and a relatively weaker Region 1 current system. Both models predict the existence of the Region 0 or the cusp currents (Iijima & Potemra, 1976b) between  $80^\circ$  and  $84^\circ$  MLAT, which are directed upward (downward) for  $B_y$  positive (negative) conditions. Another prominent feature is the impact of season. Both models clearly show stronger currents in the summer hemisphere, for all clock angles, especially on the dayside. For example, the NBZ currents are observed poleward of  $80^\circ$  MLAT, exceeding  $0.4 \mu\text{A}/\text{m}^2$  during summer. During winter, they shift slightly equatorward to  $\sim 80^\circ$  MLAT and have a much narrower latitudinal width. Furthermore, the magnitudes of the NBZ currents also reduce during winter to  $\sim 0.15 \mu\text{A}/\text{m}^2$  (statistical model) and  $\sim 0.1 \mu\text{A}/\text{m}^2$  (CNN model). Similar behavior is observed in the Region 0 currents. While both models are in good overall agreement in terms of the large-scale structure of the Birkeland currents, they exhibit certain differences in terms of magnitudes and latitudinal extent.



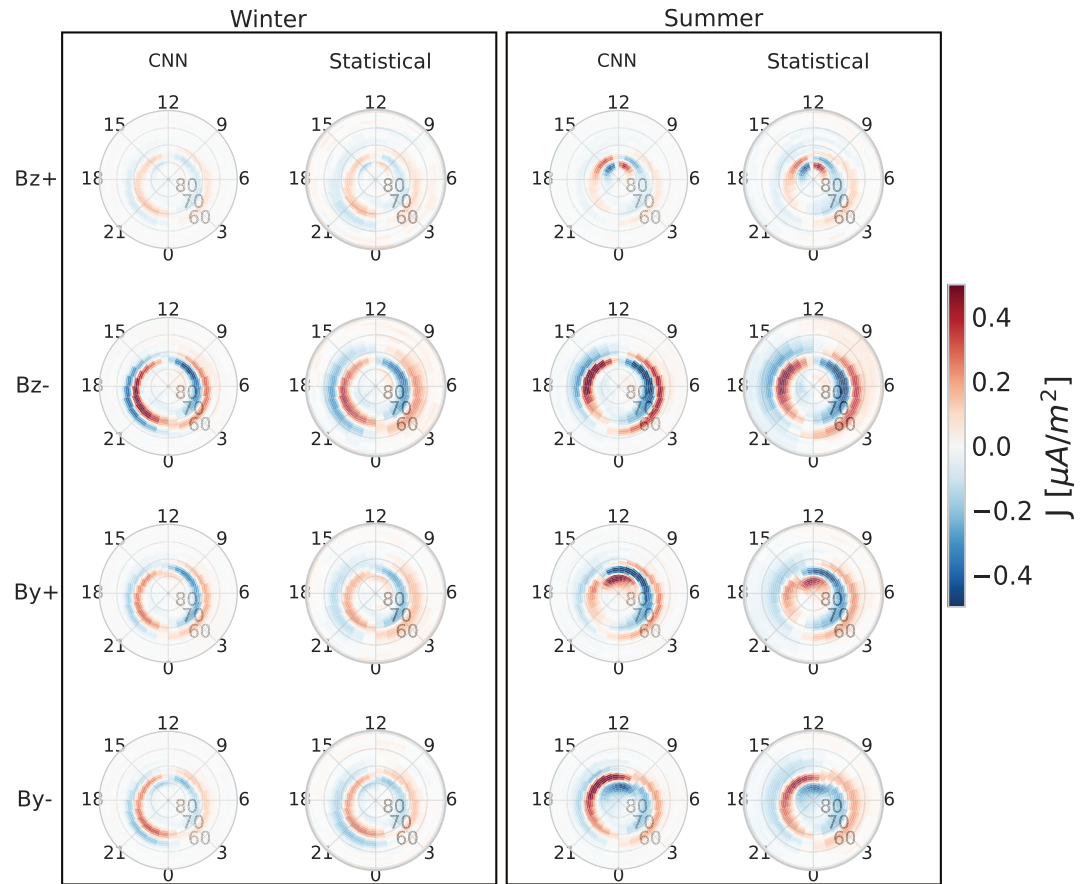


**Figure 5.** A comparison between the CNN model and statistical patterns under steady IMF conditions ( $B_t = 5$  nT) during summer (right) and winter (left) for the Northern Hemisphere. See text for details.

Specifically, the CNN model predictions of FAC density are stronger and have sharper spatial features when compared to the statistical model estimates. We will analyze the differences and similarities between these two models further in section 4.

### 3.3. Time-Dependent Analysis : Controlled Transitions

In this section, we examine the evolution of the FAC patterns predicted by our CNN model during idealized conditions when the IMF changes abruptly from one clock angle to another. In Figure 6, we present the CNN model predictions for an abrupt change from pure northward to pure southward conditions. Specifically, we present six different CNN model predictions during both summer and winter seasons, and each prediction is marked by a specific time instance relative to the transition time ( $T_{Pred} = 0$ ). The top panel shows the input time-history of IMF  $B_z$  and  $B_y$  for each  $T_{Pred}$  instance. For the first prediction ( $T_{Pred} = 0$ ), the entire 60-min IMF  $B_z$  input history is manually given a value of +5 nT, indicating an input interval when IMF  $B_z$  was purely northward. For the remaining predictions (between  $T_{Pred} = 10$  and 60 min), negative  $B_z$  values (−5 nT) are incrementally added to the input time history. For example, when  $T_{Pred} = 10$  min, the input  $B_z$  closest to the prediction time (between the 50th and the 60th minute) is replaced with −5 nT, and when  $T_{Pred} = 20$  min, the last 20 min are replaced with −5 nT. We repeat this until the entire  $B_z$  input history is replaced with a value of −5 at  $T_{Pred} = 60$  min, indicating a period when IMF was southward throughout. To segregate the impact of IMF  $B_z$ , the remaining input parameters are substituted with average values listed in Table 1. The bottom panels show global maps of FAC distributions predicted by the CNN model at different  $T_{Pred}$  values, for both winter (left) and summer (right). We note that when  $B_z$  is purely northward ( $T_{Pred} = 0$ ), the CNN model shows an NBZ current system during both seasons; however, the NBZ currents are stronger in summer ( $>0.4 \mu\text{A}/\text{m}^2$ ) compared to winter ( $<0.15 \mu\text{A}/\text{m}^2$ ). As we move from

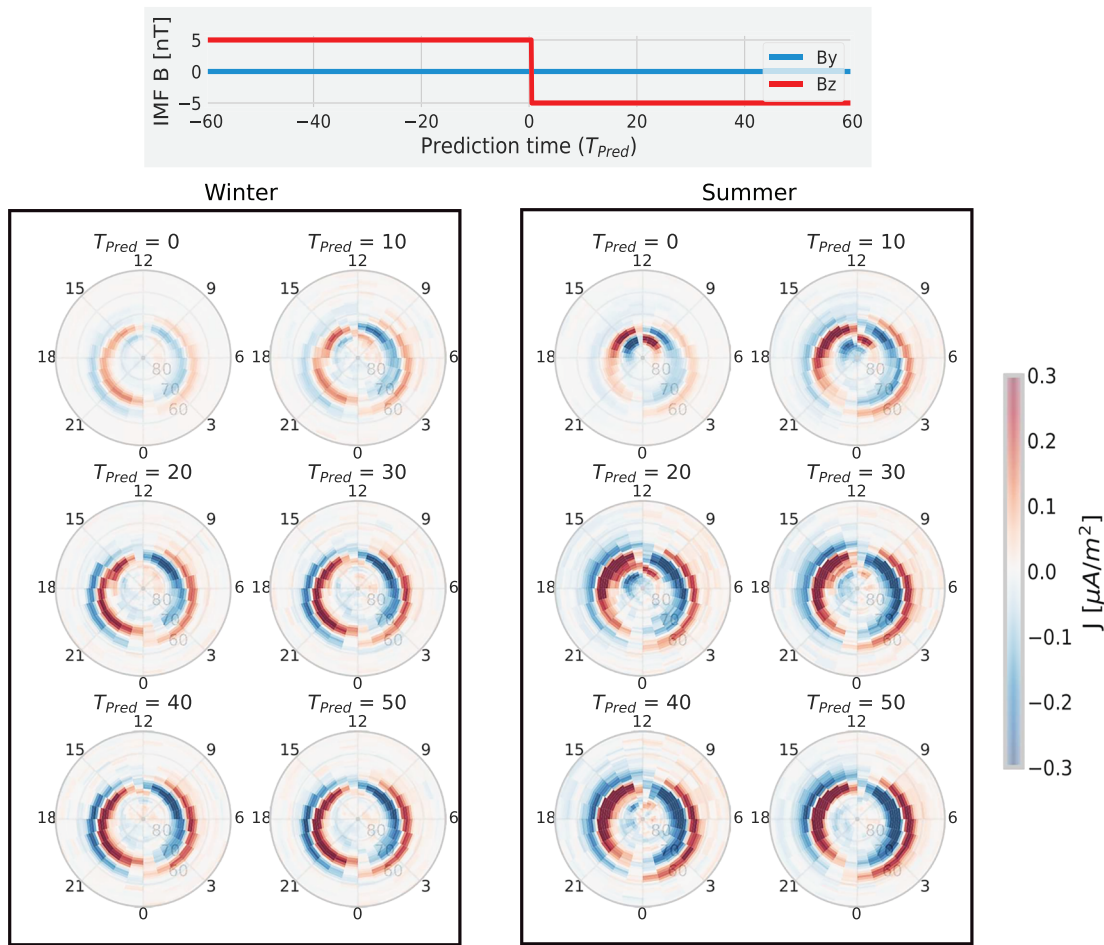


**Figure 6.** Time evolution of FACs predicted by the CNN model during a simulated time interval, when IMF Bz changed from a pure northward orientation to pure southward. The top panel shows the history of IMF Bz and By input to the model at different prediction times ( $T_{Pred}$ ). The predictions by the model during winter (bottom left) and summer (bottom right) for Northern Hemisphere are shown for different  $T_{Pred}$ . See text for details.

dominant Bz positive to Bz negative conditions, the NBZ current system slowly dissipates and a strong Region 1/Region 2 current system develops by  $T_{Pred} = 50$  min with current densities exceeding  $0.6 \mu A/m^2$ .

The temporal details of the FAC evolution to a sudden southward turning are illustrated in Figure 7, which presents MLAT versus  $T_{Pred}$  color-coded by FAC densities at 10 MLT (top), 14 MLT (middle), and 21 MLT (bottom), for both summer and winter. The NBZ currents are located on the dayside, typically between 9 and 15 MLTs (Iijima et al., 1984). In the figure, we chose to focus our analysis on 10 and 14 MLTs for further examination since the NBZ currents are most prominent in this region and to cover both the prenoon and postnoon sectors to study their temporal behavior. With 10 and 14 MLTs, we can examine the dynamics of dayside FACs, so we chose 21 and 3 MLTs to analyze the behavior of nightside FACs. In particular, we will compare the differences in the time scales of Region 1 FACs between the dayside and the nightside (e.g., Snekvik et al., 2017). Note that the NBZ currents located poleward of  $80^\circ$  MLAT, at 10 and 14 MLTs, take  $\sim 50$  min to dissipate in summer. However, this reconfiguration time is much shorter in winter, when the currents take less than 30 min to dissipate in both the dawn and dusk sectors. In short, Figures 6 and 7 clearly indicate that the response of FACs to a change in IMF Bz orientation varies with both MLT and season. We will further discuss this behavior and compare these results with previous studies in section 4.

We now examine the time scales associated with the reconfiguration of FACs in response to sudden northward to southward IMF turnings. This is shown in Figure 8. The top panels apply to a sudden southward turning (see Figures 6 and 7), while the bottom panels apply to a sudden northward turning. The

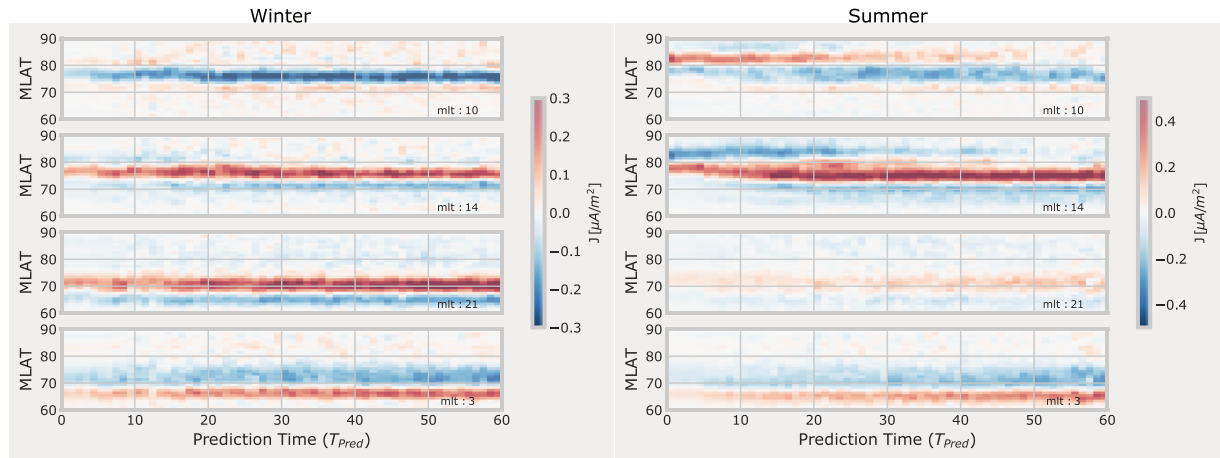


**Figure 7.** Latitude versus time plot depicting the variations in current densities at different MLTs for the prediction times indicated in Figure 6.

evolution of integrated downward NBZ currents ( $\Sigma J_{NBZ}^{\downarrow}$ ) in the left panels and the integrated upward Region 1 currents ( $\Sigma J_{R1}^{\uparrow}$ ) in the right panels are shown at selected MLTs as a function of  $T_{Pred}$ . We calculate the integrated NBZ currents by summing up the upward (positive) or downward (negative) current values above 80° MLAT at the corresponding MLT. The actual sign of the NBZ currents is determined by manual inspection. Similarly, the integrated Region 1 currents are estimated by summing up the currents between 60° and 80° MLAT, and to filter out Region 2 FACs from our calculations, we only add up

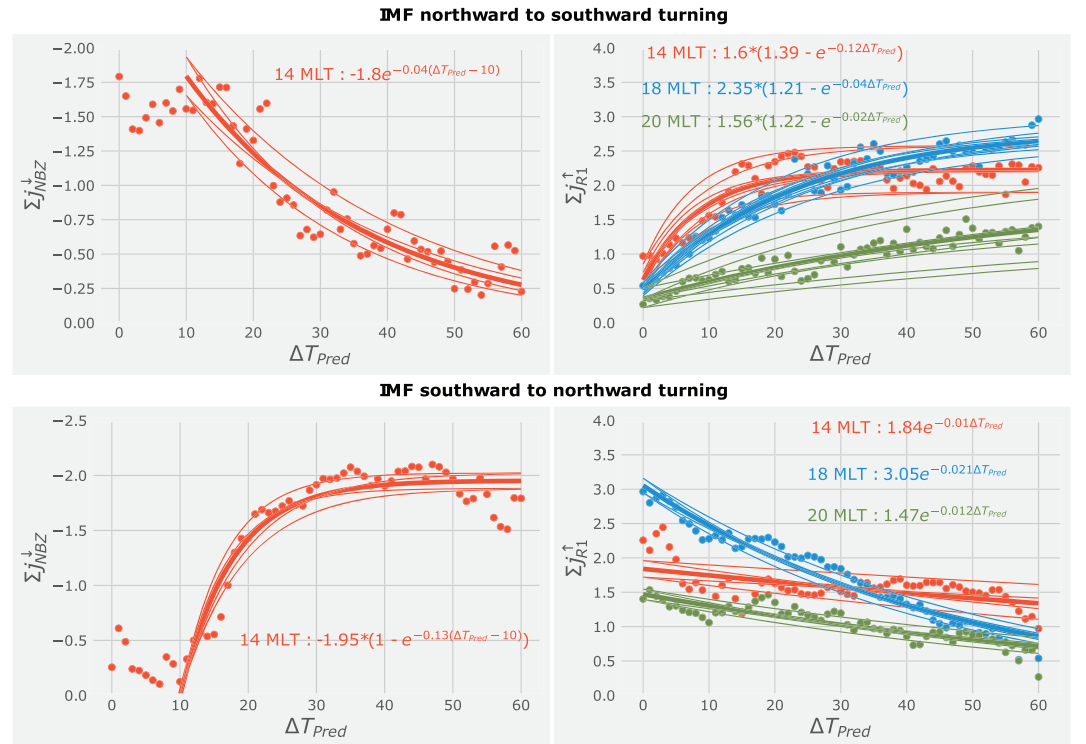


**Figure 8.** Time scales associated with decay/growth of FACs when IMF Bz turns from a northward orientation to southward (top panels) and vice versa (bottom panels) during summer. The left panels show the decay(top)/growth(bottom) rates of the integrated downward directed NBZ currents (14 MLT), and the right panels show the growth(top)/decay(bottom) rates of integrated Region 1 currents. The family of curves showing 2-sigma (standard deviation) errors in the fits are also overlaid as thin solid lines.

currents which have the opposite sense to NBZ currents at that MLT. Exponential fits for the data are shown in the figure which are used to estimate the e-folding times. Since we analyze the time scales associated with the response in FACs, we also show the family of curves marking the 2-sigma (standard deviation) error regions for the fits. As expected, when IMF turns southward after a prolonged period of northward orientation  $\Sigma J_{NBZ}^{\downarrow}$  decays, whereas the  $\Sigma J_{R1}^{\uparrow}$  grows and vice-versa for a northward turning. However, it is interesting that these currents change with e-folding times that vary with MLT. For example, when IMF turns southward, we find that  $\Sigma J_{NBZ}^{\downarrow}$  at 14 MLT fades with an e-folding time of  $\sim 25$  min, while the  $\Sigma J_{R1}^{\uparrow}$  in the noon sector (14 MLT) has the fastest e-folding time of  $\sim 8.5$  min, which progressively increases to  $\sim 45$  min at 20 MLT. Similarly, for a northward turning,  $\Sigma J_{NBZ}^{\downarrow}$  at 14 MLT increases with an e-folding time of  $\sim 8$  min, whereas  $\Sigma J_{R1}^{\uparrow}$  decrease with e-folding times between 0.8 and 1.6 hr. We can also observe from the figure that  $\Sigma J_{NBZ}^{\downarrow}$  responds after a time-lag of  $\sim 10$  min when compared to  $\Sigma J_{R1}^{\uparrow}$ . This behavior could be attributed to the differences in the location of the reconnection sites on the magnetopause. Namely, magnetic reconnection during southward Bz (driving Region 1 currents) is expected to occur near the subsolar point, whereas during northward Bz (driving NBZ currents), reconnection is expected to occur poleward of the cusp (Crooker, 1979). The time delayed response of the NBZ currents can thus be attributed to the extra time required for the sheath plasma to carry the IMF from the subsolar point to the reconnection site poleward of the cusp. This result is consistent with Maimaiti et al. (2017), who found that a change in ionospheric convection due to a northward Bz turning was delayed by 10 min compared to that for a By change and attributed this difference to the extra time required for sheath flows to reach the high latitude reconnection site.

We now examine the impact of a change in IMF By orientation on the FAC patterns using similar techniques. Figure 9 shows the CNN model predictions to manually simulated input periods representing a change in IMF By from dominant positive to negative conditions, in the same format as Figure 6. When the input time interval is dominated by a positive By ( $T_{Pred} = 0$  and 10), upward directed cusp currents are observed poleward of  $80^{\circ}$  MLAT during summer and just equatorward of  $80^{\circ}$  MLAT during winter. These cusp currents are stronger in summer, reaching a magnitude of  $\sim 0.5 \mu A/m^2$ , whereas during winter, a weaker current system with a magnitude of  $\sim 0.15 \mu A/m^2$  is observed. We note that as IMF By starts turning increasingly negative, the upward directed cusp current system dissipates and downward directed currents start to form after  $T_{Pred} = 10$  min. We further examine this reconfiguration time at different MLTs in Figure 10, which shows a plot of  $T_{Pred}$  versus MLAT at dawn (6), dusk (18), and noon (12) MLTs, in the same format as Figure 7. Our motivation through this figure is to analyze the impact of IMF By, and therefore, we chose a different set of MLTs here when compared to Figure 7. Specifically, we chose 6, 12, and 18 MLTs since IMF By is expected to drive the cusp currents and have a significant impact across the entire dayside spanning from dawn to dusk (Iijima & Potemra, 1976b). In the noon sector (middle panels), the cusp currents are clearly observed during both winter and summer and respond immediately (within 10 min) to a change in IMF By. Moreover, similar to the observations in Figure 9, upward directed cusp currents are present even at 6 MLT for By positive conditions in summer. However, during winter, these currents do not extend beyond 9 MLT and therefore are not observed in the figure. We also note that after  $T_{Pred} = 10$  min when By turns increasingly negative, the upward cusp currents reconfigure into a downward directed system and begin to intensify and expand in latitudinal width especially in the summer hemisphere.

The rate of change of the integrated cusp currents ( $\Sigma J_{cusp}$ ) and the corresponding reconfiguration times in response to a change in IMF By from a positive to negative orientation (see Figures 9 and 10) are presented in Figure 11 (similar format as Figure 8). As in Figure 8, the integrated cusp currents are calculated by summing current values above  $80^{\circ}$  MLAT. When compared to summer, the cusp currents are much weaker during winter, and therefore, we limit our analysis to summer season in Figure 11. Similar to the behavior observed with the IMF Bz transitions (Figure 8), we find that the upward directed  $\Sigma J_{cusp}$  decrease and the downward directed cusp currents increase in an exponential manner. We find that the e-folding times associated with a decrease in upward directed  $\Sigma J_{cusp}$  ( $\sim 11$  min) and increase in downward directed  $\Sigma J_{cusp}$  ( $\sim 14$  min) are roughly similar, and the downward  $\Sigma J_{cusp}$  appear after a 10-min delay. It is important to note that while the downward  $\Sigma J_{cusp}$  becomes prominent in our model predictions after a time delay of  $\sim 10$  min, it is possible that certain limitations in the AMPERE data set as well the model itself can have an impact on our results. For example, the AMPERE data set has a temporal resolution of 10 min and a spatial resolution of  $\sim 2$  hr in MLT, and as a result, smaller scale features may not be reproduced by our model. Similarly, the



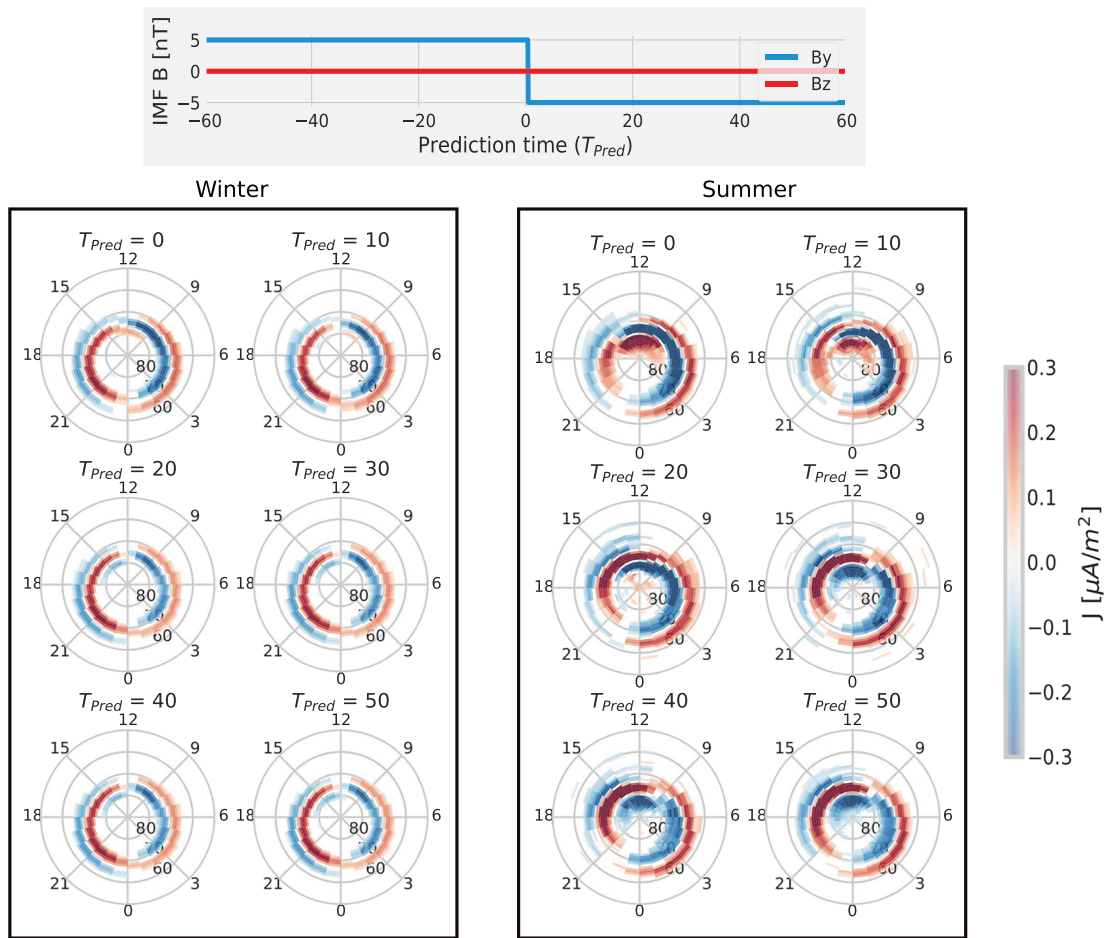


**Figure 9.** Same format as Figure 6 but for a simulated event indicating a change in  $B_y$  from positive to negative.

AMPERE FACs with relatively low magnitude (typically  $<0.2 \mu A/m^2$ ) are not reliable because of the noise level in the magnetometers used to derive them ( $>50$  nT). Such factors may influence some of our results. Later, we will compare our model predictions of FAC response to IMF transitions with observations from earlier studies.

So far, we examined the response of FACs to an abrupt change in IMF  $B_z$  and  $B_y$ . It should be noted that the relaxation time scale of the FACs depends on other factors in addition to IMF and local time. For example, if

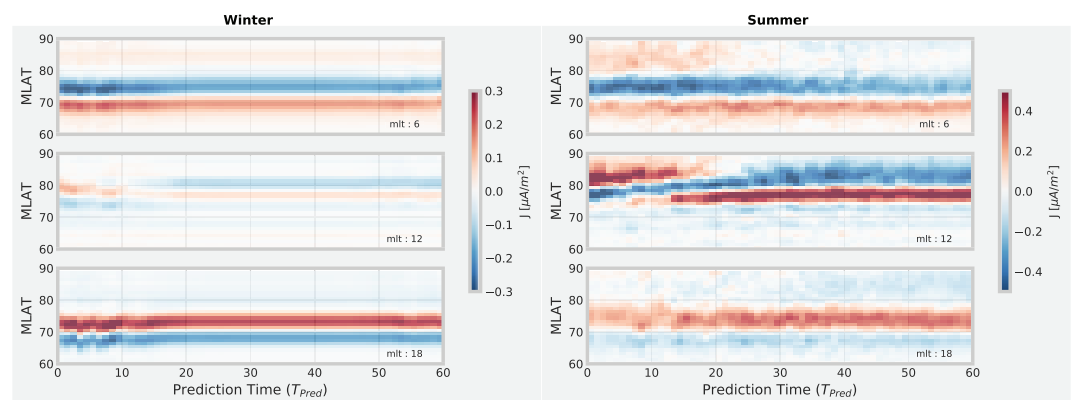


**Figure 10.** Same as Figure 7 but for a simulated event indicating a change in  $B_y$  from positive to negative.

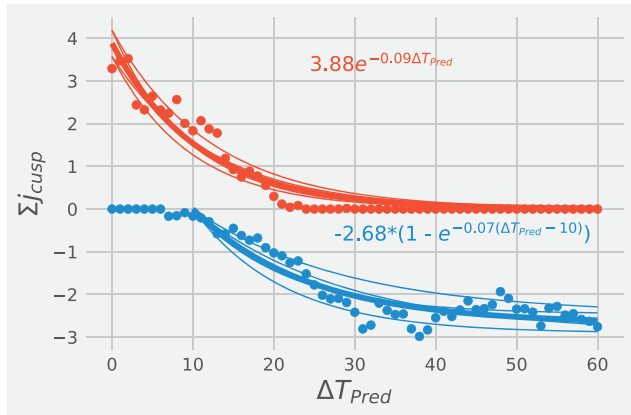


**Figure 11.** The decay (growth) rates of integrated upward (downward) directed cusp currents at 12 MLT for a change in IMF By orientation from positive to negative during summer. The best fit exponential curves for the data along with the fitting parameters is also shown in the plot. Thin solid lines show the family of curves indicating 2-sigma errors in the fit.

we increase the solar wind speed ( $V_x$ ) from 400 to 800 km/s, the e-folding time of  $\Sigma J_{R1}$  for the Bz turning from +5 to −5 nT (Figure 8) decrease from ~8–52 min to ~6–36 min. Similarly, for the IMF By transition in Figure 11, the e-folding times of  $\Sigma J_{Cusp}$  decrease from 14 to 9 min as  $V_x$  increases from 400 to 800 km/s. However, unlike the behavior observed during a southward Bz turning, we find that the e-folding times increase with increasing  $V_x$  during a northward Bz transition (Figure 8). When  $V_x$  is 400 km/s, e-folding times of  $\Sigma J_{R1}$  vary between 0.8 and 2 hr and as  $V_x$  increases to 800 km/s, the e-folding times increase to ~2.5–5.8 hr. We attribute this behavior to increased solar wind-magnetosphere coupling during periods of enhanced  $V_x$  (Newell et al., 2007), which can drive stronger  $\Sigma J_{R1}$  and thereby increase their dissipation time scales.

Lastly, we will analyze the response of our model to a “simulated” substorm interval. Similar to the previous analysis shown in Figures 6 and 9, we set all the input parameters except SML index to a constant value and vary the SML index. The results of our simulation are presented in Figure 12. We present six different CNN model predictions during summer, and each prediction is marked by a specific time ( $T_{Pred}$ ) instance relative to the transition time. The top panel shows the input time-history of

the SML index (the remaining input parameters are substituted with average values). For the first prediction at  $T_{Pred} = 0$ , the entire 60-min history of SML is set to 0, after which SML suddenly drops to −500 and stays at that value until  $T_{Pred} = 30$  min, simulating the onset and the expansion phases. Finally, between  $T_{Pred} = 30$  and 60 min, we simulate a recovery phase by turning the value of SML back to 0. We can see the response of our model at 10-min intervals of  $T_{Pred}$  in the bottom panel. We can note two main features from our model’s response to the “simulated” substorm interval. First, we find that the nightside currents intensify and

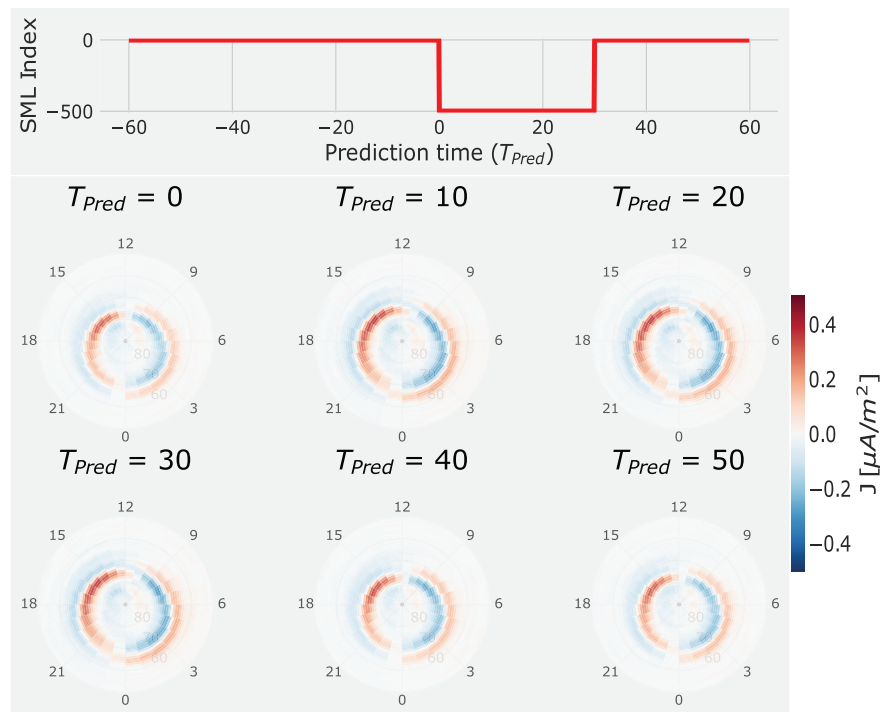


**Figure 12.** Time evolution of FACs predicted by the CNN model during a simulated substorm interval, when the SML index dropped from 0 to −500 and recovered back to 0 after a period of 30 min. The top panel shows the history of SML input to the model at different prediction times ( $T_{Pred}$ ). The predictions by the model during summer are shown for different  $T_{Pred}$  in the bottom panel. See text for details.

expand, in immediate response to a drop in SML index and later subside during the “simulated” recovery phase, beginning at  $T_{Pred} = 40$  min, as expected during a substorm interval due to an increase in nightside reconnection rate (Clausen, Milan, et al., 2013; Milan et al., 2018). Second, we find an increase in the area of the polar cap/R1-oval indicating an increase (Clausen, Baker, et al., 2013) after the onset of a substorm, which later recedes back to its original state during the recovery phase. This behavior is consistent with the expanding-contracting polar cap (ECPC) paradigm (Cowley & Lockwood, 1992), which has been reported in previous studies (Clausen, Baker, et al., 2013; Clausen, Milan, et al., 2013; Coxon et al., 2017). Finally, we can note that the signature of the upward directed currents associated with the SCW near midnight is more prominent compared to the downward directed currents. This is consistent with a few previous studies that have noted the upward portion of the SCW in the west is typically stronger and more persistent than the downward portion in the east (Clausen, Milan, et al., 2013; Hoffman et al., 1994). The behavior was attributed to the fact that in the evening sector, upward directed current closes with both the westward and eastward electrojets.

#### 4. Discussion

In the previous sections, we presented a CNN architecture to model the spatio-temporal dynamics of AMPERE FACs in the Northern Hemisphere. We showed that our model was consistent with the standard modeling of the FACs under quasi-static conditions and successfully expressed several large-scale features of the Birkeland current system. However, the advantage of using our CNN model over bin-averaged statistical patterns was most apparent when IMF changed its orientation abruptly, driving an MLT-dependent reconfiguration in the FAC patterns. In this section, we further discuss our findings and compare them with observations from previous studies.

We begin with a comparison between the CNN and bin-averaged statistical models to determine the validity of our CNN model when IMF and solar wind are stable. From Figure 5, we note that our CNN model is largely consistent with the bin-averaged patterns. Specifically, the CNN model is able to successfully express previously reported features such as the Region 1/Region 2 current system (Anderson et al., 2008; Iijima & Potemra, 1976a; Papitashvili et al., 2002) during predominantly southward Bz conditions and the NBZ currents (Weimer, 2001) during positive Bz conditions. Moreover, our CNN model also captures the strong dependence of the dayside cusp currents on the sign of IMF By (Fujii et al., 1981; Green et al., 2009; Iijima & Potemra, 1976a, 1976b; Ohtani et al., 1976b), with  $B_y > 0$  ( $< 0$ ) driving upward (downward) cusp currents near noon. Finally, the strong influence of season on the large-scale morphology and intensity of the currents predicted by our model is consistent with previous studies (Fujii et al., 1981; Green et al., 2009; Laundal, Finlay, et al., 2018; Ohtani et al., 2005). The peak Region 1 currents in the dusk region are observed in the postnoon sector during summer and they shift to the premidnight sector during winter. Such a redistribution of peak FACs is not observed on the dawnside. This behavior can be attributed to the significant diffuse electron precipitation in the prenoon region, which is observed independent of seasons (Laundal et al., 2016; Newell et al., 2010) and is consistent with previous observations (Ohtani et al., 2005). One important difference that we find between the CNN model and the statistical model is that the currents predicted by the CNN model are stronger and more sharply defined in latitude when compared with the bin-averaged patterns presented in this study and earlier studies (Green et al., 2009; Iijima & Potemra, 1976a). We attribute this behavior to the fact that the statistical patterns are averaged over a wider set of geomagnetic conditions and do not take into account a time history of geomagnetic activity. As a result, the statistical patterns have a tendency to smear features over a wider latitudinal range rendering weaker magnitudes. This behavior can be observed in Figure 2, where the currents determined by the CNN model (panel c) have a much smaller latitudinal spread compared to the statistical patterns (panel a) and are in good agreement with the actual data (panel b). To summarize, a comparison with bin-averaged statistical patterns shows that our CNN model successfully replicates several important large-scale features of the Birkeland current system under quasi-static IMF conditions, thereby validating its ability to express the impact of important parameters on FAC patterns. The Harang discontinuity is known to influence the night auroral FAC structure (He, Vogt, et al., 2012; Iijima & Potemra, 1978). We find two important features of Harang discontinuity in our results. First, the Harang discontinuity is located at earlier MLTs when IMF By is positive ( $T_{Pred} = 0$  min in Figure 9), whereas it shifts to later MLTs when IMF By turns negative ( $T_{Pred} = 50$  min in Figure 9). This is consistent with previous reports (He, Vogt, et al., 2012; Rodger et al., 1984) and has

been attributed to the longitudinal shift in field lines associated with IMF By “penetration” into the magnetosphere (Rodger et al., 1984). Second, a small shift in the location of the Harang discontinuity is also observed with season; namely, it shifts to later MLTs in winter when compared to summer (see Figures 5, 6, and 9). The standard paradigm says that the Harang discontinuity results from a dawn/dusk asymmetry in total energetic plasma content across the magnetotail, which exists because the gradient/curvature drift depletes dawnside flux tubes of energetic ions (Erickson et al., 1991). Our observations suggest ionospheric conductivity may also play an important role in controlling the dynamics of Harang discontinuity.

We now discuss the impact of abrupt changes in IMF on FACs. The results presented in section 3 suggest that the response of FACs to variations in IMF and solar wind depends on MLT and season. Here, by response in FACs we mean the first noticeable change in the strength of the FACs to an abrupt change in the IMF. Please note that this is different from the total reconfiguration time, which is the total time taken by the FACs to change from one state to another (e.g., from a fully southward Bz pattern to a fully northward Bz pattern). In Figures 2–4, we find that after a southward turning of IMF Bz, the response of the FACs is strongest and quickest on the dayside and progresses toward the nightside after a time delay of a few tens of minutes. We examine Figures 6 and 7 to explore any seasonal dependencies to this behavior. From the summer FAC maps in Figure 6, we can note that the FACs on the dayside start to intensify almost immediately near the noon sector (by  $T_{Pred} = 10$  min), whereas on the nightside, the intensification in FACs begins after a time delay (when  $T_{Pred} = 20$ –30 min). In contrast, from the winter FAC maps, we can clearly note that by  $T_{Pred} = 10$  min, the FACs begin to intensify on both the dayside and the nightside almost simultaneously. These observations from our CNN model suggest that during winter, the response of FACs to changes in IMF is globally simultaneous, similar to the observations of ionospheric convection presented in Ridley et al. (1997) and Ruohoniemi and Greenwald (1998), whereas a time delay is associated with the response during summer away from noon similar to the observations presented in Lockwood et al. (1986) and Saunders et al. (1992). The decrease in magnitude of the response away from the noon sector predicted by our CNN model is consistent with the recent observations presented in Snekvik et al. (2017). In summary, our model predictions indicate that the response of FACs to changes in IMF is complex and depends on several factors such as season and time history of IMF, which describe the preconditioned state of the ionosphere. In some cases, the response is found to be globally simultaneous, and in others, a time delay between dayside and nightside response is observed. Further analysis using a large statistical set of events under different geomagnetic conditions is required to fully quantify its nature.

Another crucial observation from our CNN model is that the FACs decay exponentially when IMF Bz/By changes abruptly, as observed in Figures 8 and 11. Such behavior was previously reported by Moretto et al. (2018), who examined AMPERE FACs during events of northward IMF turnings and found an exponential decay in the total hemispheric current with a median e-folding time of 1.1 hr. In comparison, we find that the e-folding time depends on MLT and typically varies between 0.8 and 1.6 hr (Figure 8) when IMF turns northward. Furthermore, we find that the FAC growth rates are faster than their decay rates. For example, as observed in Figure 8, following a southward turning of IMF, the Region 1 currents grow rapidly with the e-folding times, gradually increasing from noon to the midnight sector (varying between 0.1 and 0.7 hr). Finally, another important feature we can observe from Figures 7 and 10 is the variability in the current patterns with season. For example, in Figure 7, the NBZ currents are very faint during winter, whereas during summer, they are much stronger and noticeable. Moreover, unlike the winter season where the NBZ currents dissipate within 20–30 min, they take up to 50 min to completely dissipate during summer. Likewise, the upward cusp currents near 12 MLT in Figure 10 take longer in summer (>20 min) to dissipate as compared to winter (<10 min). Our observations are in good agreement with Moretto et al. (2018), who suggested that a weaker line-tying of the magnetospheric field lines during winter can result in an easier and quicker unwinding of current-carrying flux tubes and therefore a faster decay period.

One advantage of using a deep learning model is that we can isolate and analyze the impact of different input features by creating synthetic inputs. We took advantage of this capability to estimate the time scales of FAC response and reconfiguration through simulated IMF transitions. We found that for a northward turning of Bz, the NBZ currents develop with an e-folding time of  $\sim 8$  min and take  $\sim 50$  min to fully develop, whereas R1 FACs decrease over a period of 60 min or more on the dayside (Figure 8). These time scales are in agreement with Milan et al. (2018), who used principal component analysis and reported that NBZ currents



typically take between 45 and 90 min to fully develop. In comparison, McPherron et al. (2018) reported the peak response of AMPERE-derived dayside currents to an optimum coupling function (OPN) (McPherron et al., 2015) as 40 min and nightside currents as 60 min. Milan et al. (2018) suggested that such time scales could be interpreted as a signature of the expanding/contracting polar cap (ECPC) paradigm (Cowley & Lockwood, 1992). Finally, the response of FACs to sudden transitions in IMF can be used to study inner magnetosphere shielding. During periods of large and rapid fluctuations of IMF, the inner magnetosphere shielding mechanism (Wolf et al., 2007) is expected to be perturbed, resulting in either undershielding or overshielding of the inner magnetosphere (Jaggi & Wolf, 1973; Sazykin, 2000). For example, when IMF Bz suddenly turns southward, the cross-tail electric field should increase rapidly, whereas Region 2 FACs (and thereby shielding electric field) takes time to readjust, allowing the “penetration” of convection electric fields to subauroral latitudes. The Region 1 FACs are expected to respond immediately when IMF Bz changes abruptly, whereas Region 2 FACs are expected to respond after a time lag. However, a closer examination of Figures 6 and 10 shows that our model predicts a nearly simultaneous formation of Region 1 and Region 2 currents after the southward turning of IMF Bz. This finding is in agreement with recent AMPERE-based studies (Anderson et al., 2014, 2018), which show that the Region 1 and Region 2 FACs develop together first on the dayside, later on the nightside, and finally develop into a complete Region 1/2 FAC pattern covering all MLTs. In such a scenario, it was suggested that penetration electric fields could also be a result of fringing fields originating from local time gradients in currents (Anderson et al., 2014, 2018). A detailed investigation of the relative differences between the evolution of Region 1 and 2 FACs will be pursued in a later effort.

## 5. Conclusions

In this paper, we present the first application of deep learning (ResNet CNN) architecture to model the dynamics of the Birkeland current system in the Northern Hemisphere. The model uses a 1-hr history of solar wind and IMF parameters ( $V_x$ ,  $N_p$ ,  $B_x$ ,  $B_y$ , and  $B_z$ ) along with geomagnetic indices (SML, SMU, Sym-H, and Asym-H) and F10.7 flux to model the FACs. Our CNN model was trained on global FAC patterns provided by the AMPERE project between 2010 and 2016. A comparison with statistical patterns bin-averaged by IMF Bz and  $B_y$  and by season showed that our CNN model successfully captured several prominent features of the Birkeland current system such as the Region 1/Region 2, NBZ, and the cusp currents, along with their seasonal variability, under steady solar wind conditions. However, when the IMF was variable and changed its orientation abruptly, our CNN model outperformed the statistical model in capturing the time-dependent evolution of FACs at different MLTs. Our model predictions suggest that FACs decrease/grow in an exponential manner in response to an abrupt change in IMF. For example, when IMF turns northward, the Region 1 currents fade with an e-folding time that varies between 0.8 and 1.6 hr depending on MLT, whereas the NBZ currents grow rapidly with an e-folding time of  $\sim 8$  min. These results demonstrate that training deep learning models on large and nearly continuous data sets such as AMPERE can provide new insights into the dynamics of solar wind-magnetosphere-ionosphere coupling, and such models can outperform traditional bin-averaged statistical patterns under realistic and variable IMF/solar wind parameters.

## Data Availability Statement

The Iridium-derived AMPERE data used in this paper can be obtained from the AMPERE Science Center (at <http://ampere.jhuapl.edu/>). The OMNI data used in this paper can be obtained from NASA/GSFC's Space Physics Data Facility's CDAweb service (at <http://cdaweb.gsfc.nasa.gov/>).

## References

- Anderson, B. J., Korth, H., Waters, C. L., Green, D. L., Merkin, V. G., Barnes, R. J., & Dyrd, L. P. (2014). Development of large-scale Birkeland currents determined from the active magnetosphere and planetary electrodynamics response experiment. *Geophysical Research Letters*, 41, 3017–3025. <https://doi.org/10.1002/2014GL059941>
- Anderson, B. J., Korth, H., Waters, C. L., Green, D. L., & Stauning, P. (2008). Statistical Birkeland current distributions from magnetic field observations by the Iridium constellation. *Annales Geophysicae*, 26(3), 671–687. <https://doi.org/10.5194/angeo-26-671-2008>
- Anderson, B. J., Olson, C. N., Korth, H., Barnes, R. J., Waters, C. L., & Vines, S. K. (2018). Temporal and spatial development of global Birkeland currents. *Journal of Geophysical Research: Space Physics*, 123, 4785–4808. <https://doi.org/10.1029/2018JA025254>

## Acknowledgments

We thank the National Science Foundation for support under Grants AGS-1822056 and AGS-1839509. The authors acknowledge Advanced Research Computing (<https://www.arc.vt.edu/>) at Virginia Tech for providing computational resources and technical support that have contributed to the results reported within this paper. We thank the AMPERE team and the AMPERE Science Center for providing the Iridium-derived data products. The majority of analysis and visualization were completed with the help of free, open-source software tools such as matplotlib (Hunter, 2007), IPython (Pérez & Granger, 2007), pandas (McKinney, 2010), and others (Millman & Aivazis, 2011). The code for our deep learning model and trained model weights are now open-sourced (Kunduri, 2020).

- Anderson, B. J., Takahashi, K., Kamei, T., Waters, C. L., & Toth, B. A. (2002). Birkeland current system key parameters derived from Iridium observations: Method and initial validation results. *Journal of Geophysical Research*, 107(A6), SMP 11–1–SMP 11–13. <https://doi.org/10.1029/2001JA000080>
- Anderson, B. J., Takahashi, K., & Toth, B. A. (2000). Sensing global Birkeland currents with Iridium engineering magnetometer data. *Geophysical Research Letters*, 27(24), 4045–4048. <https://doi.org/10.1029/2000GL000094>
- Birkeland, K. R. (1908). The Norwegian aurora borealis expedition, vol. 1902–1903, h. Aschehoug and Co., Christiania, Denmark.
- Carter, J. A., Milan, S. E., Coxon, J. C., Walach, M.-T., & Anderson, B. J. (2016). Average field-aligned current configuration parameterized by solar wind conditions. *Journal of Geophysical Research: Space Physics*, 121, 1294–1307. <https://doi.org/10.1002/2015JA021567>
- Chen, J., Zeng, G.-Q., Zhou, W., Du, W., & Lu, K.-D. (2018). Wind speed forecasting using nonlinear-learning ensemble of deep learning time series prediction and extremal optimization. *Energy Conversion and Management*, 165, 681–695. <https://doi.org/10.1016/j.enconman.2018.03.098>
- Chollet, F. (2015). Keras. <https://keras.io>
- Clausen, L. B. N., Baker, J. B. H., Ruohoniemi, J. M., Milan, S. E., Coxon, J. C., Wing, S., et al. (2013). Temporal and spatial dynamics of the Regions 1 and 2 Birkeland currents during substorms. *Journal of Geophysical Research: Space Physics*, 118, 3007–3016. <https://doi.org/10.1002/jgra.50288>
- Clausen, L. B. N., Milan, S. E., Baker, J. B. H., Ruohoniemi, J. M., Glassmeier, K.-H., Coxon, J. C., & Anderson, B. J. (2013). On the influence of open magnetic flux on substorm intensity: Ground- and space-based observations. *Journal of Geophysical Research: Space Physics*, 118, 2958–2969. <https://doi.org/10.1002/jgra.50308>
- Cowley, S. W. H., & Lockwood, M. (1992). Excitation and decay of solar wind-driven flows in the magnetosphere-ionosphere system. *Annales Geophysicae*, 10(1–2), 103–115.
- Coxon, J. C., Milan, S. E., & Anderson, B. J. (2018). A review of Birkeland current research using ampere. In A. Keiling, O. Marghitu, & M. Wheatland (Eds.), *Electric currents in geospace and beyond* (pp. 257–278). American Geophysical Union (AGU). <https://doi.org/10.1002/9781119324522.ch16>
- Coxon, J. C., Rae, I. J., Forsyth, C., Jackman, C. M., Fear, R. C., & Anderson, B. J. (2017). Birkeland currents during substorms: Statistical evidence for intensification of Regions 1 and 2 currents after onset and a localized signature of auroral dimming. *Journal of Geophysical Research: Space Physics*, 122, 6455–6468. <https://doi.org/10.1002/2017JA023967>
- Crooker, N. U. (1979). Dayside merging and cusp geometry. *Journal of Geophysical Research*, 84(A3), 951–959. <https://doi.org/10.1029/JA084iA03p00951>
- Erickson, G. M., Spiro, R. W., & Wolf, R. A. (1991). The physics of the Harang discontinuity. *Journal of Geophysical Research*, 96(A2), 1633–1645. <https://doi.org/10.1029/90JA02344>
- Erlundson, R. E., Zanetti, L. J., Potemra, T. A., Bythrow, P. F., & Lundin, R. (1988). IMF by dependence of Region 1 Birkeland currents near noon. *Journal of Geophysical Research*, 93(A9), 9804–9814. <https://doi.org/10.1029/JA093iA09p09804>
- Fawaz, H. I., Forestier, G., Weber, J., Idoumghar, L., & Muller, P.-A. (2019). Deep learning for time series classification: A review. *Data Mining and Knowledge Discovery* (pp. 1–47).
- Fujii, R., Iijima, T., Potemra, T. A., & Sugiura, M. (1981). Seasonal dependence of large-scale Birkeland currents. *Geophysical Research Letters*, 8(10), 1103–1106. <https://doi.org/10.1029/GL008i010p01103>
- Gjerloev, J. W. (2012). The SuperMAG data processing technique. *Journal of Geophysical Research*, 117, A09213. <https://doi.org/10.1029/2012JA017683>
- Glorot, X., & Bengio, Y. (2010). Understanding the difficulty of training deep feedforward neural networks. In Y. W. Teh, & M. Titterton (Eds.), *Proceedings of the Thirteenth International Conference on Artificial Intelligence and Statistics* (Vol. 9, pp. 249–256), *Proceedings of Machine Learning Research*. Chia Laguna Resort, Sardinia, Italy: PMLR.
- Green, D. L., Waters, C. L., Anderson, B. J., & Korth, H. (2009). Seasonal and interplanetary magnetic field dependence of the field-aligned currents for both Northern and Southern Hemispheres. *Annales Geophysicae*, 27(4), 1701–1715. <https://doi.org/10.5194/angeo-27-1701-2009>
- He, M., Vogt, J., Lhr, H., Sorbalo, E., Blagau, A., Le, G., & Lu, G. (2012). A high-resolution model of field-aligned currents through empirical orthogonal functions analysis (MFACE). *Geophysical Research Letters*, 39, L18105. <https://doi.org/10.1029/2012GL053168>
- He, K., Zhang, X., Ren, S., & Sun, J. (2016). Deep residual learning for image recognition. In *2016 IEEE Conference on Computer Vision and Pattern Recognition (CVPR)*. <https://doi.org/10.1109/CVPR.2016.90>
- Hoffman, R. A., Fujii, R., & Sugiura, M. (1994). Characteristics of the field-aligned current system in the nighttime sector during auroral substorms. *Journal of Geophysical Research*, 99(A11), 21,303–21,325. <https://doi.org/10.1029/94JA01659>
- Hunter, J. D. (2007). Matplotlib: A 2D graphics environment. *Computing In Science & Engineering*, 9(3), 90–95. <https://doi.org/10.1109/MCSE.2007.55>
- Iijima, T., & Potemra, T. A. (1976a). The amplitude distribution of field-aligned currents at northern high latitudes observed by Triad. *Journal of Geophysical Research*, 81(13), 2165–2174. <https://doi.org/10.1029/JA081i013p02165>
- Iijima, T., & Potemra, T. A. (1976b). Field-aligned currents in the dayside cusp observed by Triad. *Journal of Geophysical Research*, 81(34), 5971–5979. <https://doi.org/10.1029/JA081i034p05971>
- Iijima, T., & Potemra, T. A. (1978). Large-scale characteristics of field-aligned currents associated with substorms. *Journal of Geophysical Research*, 83(A2), 599–615. <https://doi.org/10.1029/JA083iA02p00599>
- Iijima, T., Potemra, T. A., Zanetti, L. J., & Bythrow, P. F. (1984). Large-scale Birkeland currents in the dayside polar region during strongly northward IMF: A new Birkeland current system. *Journal of Geophysical Research*, 89(A9), 7441–7452. <https://doi.org/10.1029/JA089iA09p07441>
- Iijima, T., & Shibaji, T. (1987). Global characteristics of northward IMF-associated (NBZ) field-aligned currents. *Journal of Geophysical Research*, 92(A3), 2408–2424. <https://doi.org/10.1029/JA092iA03p02408>
- Iyemori, T. (1990). Storm-time magnetospheric currents inferred from mid-latitude geomagnetic field variations. *Journal of Geomagnetism and Geoelectricity*, 42(11), 1249–1265. <https://doi.org/10.5636/jgg.42.1249>
- Jaggi, R. K., & Wolf, R. A. (1973). Self-consistent calculation of the motion of a sheet of ions in the magnetosphere. *Journal of Geophysical Research*, 78(16), 2852–2866. <https://doi.org/10.1029/JA078i016p02852>
- King, J. H., & Papitashvili, N. E. (2005). Solar wind spatial scales in and comparisons of hourly wind and ACE plasma and magnetic field data. *Journal of Geophysical Research*, 110, A02104. <https://doi.org/10.1029/2004JA010649>
- Kingma, D. P., & Ba, J. (2014). Adam: A method for stochastic optimization. arXiv preprint arXiv:1412.6980.
- Kunduri, B. (2020). bharatreddy/ampere\_fac\_cnn\_model v0.1. <https://doi.org/10.5281/zenodo.3872345>

- Lake, B. M., Salakhutdinov, R., & Tenenbaum, J. B. (2015). Human-level concept learning through probabilistic program induction. *Science*, 350(6266), 1332–1338. <https://doi.org/10.1126/science.aab3050>
- Lake, B. M., Ullman, T. D., Tenenbaum, J. B., & Gershman, S. J. (2017). Building machines that learn and think like people. *Behavioral and Brain Sciences*, 40, e253. <https://doi.org/10.1017/S0140525X16001837>
- Laundal, K. M., Finlay, C. C., & Olsen, N. (2016). Sunlight effects on the 3D polar current system determined from low earth orbit measurements. *Earth, Planets and Space*, 68(1), 142. <https://doi.org/10.1186/s40623-016-0518-x>
- Laundal, K. M., Finlay, C. C., Olsen, N., & Reistad, J. P. (2018). Solar wind and seasonal influence on ionospheric currents from Swarm and CHAMP measurements. *Journal of Geophysical Research: Space Physics*, 123, 4402–4429. <https://doi.org/10.1029/2018JA025387>
- Laundal, K. M., Reistad, J. P., Finlay, C. C., Stgaard, N., Tenfjord, P., Snekvik, K., & Ohma, A. (2018). Interplanetary magnetic field Bx component influence on horizontal and field-aligned currents in the ionosphere. *Journal of Geophysical Research: Space Physics*, 123, 3360–3379. <https://doi.org/10.1002/2017JA024864>
- LeCun, Y., Bengio, Y., & Hinton, G. (2015). Deep learning. *Nature*, 521(7553), 436. <https://doi.org/10.1038/nature14539>
- Liemohn, M. W., McCollough, J. P., Jordanova, V. K., Ngwira, C. M., Morley, S. K., Cid, C., et al. (2018). Model evaluation guidelines for geomagnetic index predictions. *Space Weather*, 16, 2079–2102. <https://doi.org/10.1029/2018SW002067>
- Lockwood, M., van Eyken, A. P., Bromage, B. J. I., Willis, D. M., & Cowley, S. W. H. (1986). Eastward propagation of a plasma convection enhancement following a southward turning of the interplanetary magnetic field. *Geophysical Research Letters*, 13(1), 72–75. <https://doi.org/10.1029/GL013i001p00072>
- Lysak, R. L. (1990). Electrodynamics coupling of the magnetosphere and ionosphere. *Space Science Reviews*, 52(1), 33–87. <https://doi.org/10.1007/BF00704239>
- Maimaiti, M., Kunduri, B., Ruohoniemi, J. M., Baker, J. B. H., & House, L. L. (2019). A deep learning based approach to forecast the onset of magnetic substorms. *Space Weather*, 17, 1534–1552. <https://doi.org/10.1029/2019SW002251>
- Maimaiti, M., Ruohoniemi, J. M., Baker, J. B. H., Clauer, C. R., Nicolls, M. J., & Hairston, M. R. (2017). RISR-N observations of the IMF by influence on reverse convection during extreme northward IMF. *Journal of Geophysical Research: Space Physics*, 122, 3707–3720. <https://doi.org/10.1002/2016JA023612>
- Matsuo, T., Knipp, D. J., Richmond, A. D., Kilcommons, L., & Anderson, B. J. (2015). Inverse procedure for high-latitude ionospheric electrodynamics: Analysis of satellite-borne magnetometer data. *Journal of Geophysical Research: Space Physics*, 120, 5241–5251. <https://doi.org/10.1002/2014JA020565>
- Mauk, B. H., & Zanetti, L. J. (1987). Magnetospheric electric fields and currents. *Reviews of Geophysics*, 25(3), 541–554. <https://doi.org/10.1029/RG025i003p00541>
- McKinney, W. (2010). Data structures for statistical computing in python. In S. van der Walt, & J. Millman (Eds.) *Proceedings of the 9th Python in Science Conference* (pp. 51–56). Conference SciPy.
- McPherron, R. L., Anderson, B. J., & Chu, X. (2018). Relation of field-aligned currents measured by the network of Iridium spacecraft to solar wind and substorms. *Geophysical Research Letters*, 45, 2151–2158. <https://doi.org/10.1002/2017GL076741>
- McPherron, R. L., Hsu, T.-S., & Chu, X. (2015). An optimum solar wind coupling function for the al index. *Journal of Geophysical Research: Space Physics*, 120, 2494–2515. <https://doi.org/10.1002/2014JA020619>
- Milan, S. E., Carter, J. A., Sangha, H., Laundal, K. M., Stgaard, N., Tenfjord, P., et al. (2018). Timescales of dayside and nightside field-aligned current response to changes in solar wind-magnetosphere coupling. *Journal of Geophysical Research: Space Physics*, 123, 7307–7319. <https://doi.org/10.1029/2018JA025645>
- Millman, K. J., & Aivazis, M. (2011). Python for scientists and engineers. *Computing in Science & Engineering*, 13(2), 9–12. <https://doi.org/10.1109/MCSE.2011.36>
- Moretto, T., Hesse, M., Vennerström, S., & Tenfjord, P. (2018). Estimating the rate of cessation of magnetospheric activity in AMPERE field-aligned currents. *Geophysical Research Letters*, 45, 12,713–12,719. <https://doi.org/10.1029/2018GL080631>
- Murphy, K. R., Mann, I. R., Rae, I. J., Waters, C. L., Anderson, B. J., Milling, D. K., et al. (2012). Reduction in field-aligned currents preceding and local to auroral substorm onset. *Geophysical Research Letters*, 39, L15106. <https://doi.org/10.1029/2012GL052798>
- Newell, P. T., Sotirelis, T., Liou, K., Meng, C.-I., & Rich, F. J. (2007). A nearly universal solar wind-magnetosphere coupling function inferred from 10 magnetospheric state variables. *Journal of Geophysical Research*, 112, A01206. <https://doi.org/10.1029/2006JA012015>
- Newell, P. T., Sotirelis, T., & Wing, S. (2010). Seasonal variations in diffuse, monoenergetic, and broadband aurora. *Journal of Geophysical Research*, 115, A03216. <https://doi.org/10.1029/2009JA014805>
- Ohtani, S., Ueno, G., & Higuchi, T. (2005). Comparison of large-scale field-aligned currents under sunlit and dark ionospheric conditions. *Journal of Geophysical Research*, 110, A09230. <https://doi.org/10.1029/2005JA011057>
- Papitashvili, V. O., Christiansen, F., & Neubert, T. (2002). A new model of field-aligned currents derived from high-precision satellite magnetic field data. *Geophysical Research Letters*, 29(14), 28–1–28–4. <https://doi.org/10.1029/2001GL014207>
- Pérez, F., & Granger, B. E. (2007). IPython: A system for interactive scientific computing. *Computing in Science and Engineering*, 9(3), 21–29. <https://doi.org/10.1109/MCSE.2007.53>
- Pettigrew, E. D., Shepherd, S. G., & Ruohoniemi, J. M. (2010). Climatological patterns of high-latitude convection in the Northern and Southern Hemispheres: Dipole tilt dependencies and interhemispheric comparisons. *Journal of Geophysical Research*, 115, A07305. <https://doi.org/10.1029/2009JA014956>
- Potemra, T. A. (1985). Field-aligned (Birkeland) currents. *Space Science Reviews*, 42(3), 295–311. <https://doi.org/10.1007/BF00214990>
- Qin, Y., Song, D., Chen, H., Cheng, W., Jiang, G., & Cottrell, G. W. (2017). A dual-stage attention-based recurrent neural network for time series prediction. *CoRR*, abs/1704.02971.
- Richmond, A. D. (1992). Assimilative mapping of ionospheric electrodynamics. *Advances in Space Research*, 12(6), 59–68. [https://doi.org/10.1016/0273-1177\(92\)90040-5](https://doi.org/10.1016/0273-1177(92)90040-5)
- Ridley, A. J., Lu, G., Clauer, C. R., & Papitashvili, V. O. (1997). Ionospheric convection during nonsteady interplanetary magnetic field conditions. *Journal of Geophysical Research*, 102(A7), 14,563–14,579. <https://doi.org/10.1029/97JA00940>
- Ridley, A. J., Lu, G., Clauer, C. R., & Papitashvili, V. O. (1998). A statistical study of the ionospheric convection response to changing interplanetary magnetic field conditions using the assimilative mapping of ionospheric electrodynamics technique. *Journal of Geophysical Research*, 103(A3), 4023–4039. <https://doi.org/10.1029/97JA03328>
- Rodger, A. S., Cowley, S. W. H., Brown, M. J., Pinnock, M., & Simmons, D. A. (1984). Dawn-dusk (y) component of the interplanetary magnetic field and the local time of the Harang discontinuity. *Planetary and Space Science*, 32(8), 1021–1027. [https://doi.org/10.1016/0032-0633\(84\)90058-8](https://doi.org/10.1016/0032-0633(84)90058-8)
- Rumelhart, D. E., Hinton, G. E., & Williams, R. J. (1986). Learning representations by back-propagating errors. *Nature*, 323(6088), 533–536. <https://doi.org/10.1038/323533a>

- Ruohoniemi, J. M., & Greenwald, R. A. (1996). Statistical patterns of high-latitude convection obtained from Goose Bay HF radar observations. *Journal of Geophysical Research*, 101(A10), 21,743–21,763. <https://doi.org/10.1029/96JA01584>
- Ruohoniemi, J. M., & Greenwald, R. A. (1998). The response of high-latitude convection to a sudden southward IMF turning. *Geophysical Research Letters*, 25(15), 2913–2916. <https://doi.org/10.1029/98GL02212>
- Ruohoniemi, J. M., Shepherd, S. G., & Greenwald, R. A. (2002). The response of the high-latitude ionosphere to IMF variations. *Journal of Atmospheric and Solar-Terrestrial Physics*, 64(2), 159–171. [https://doi.org/10.1016/S1364-6826\(01\)00081-5](https://doi.org/10.1016/S1364-6826(01)00081-5)
- Saunders, M. A. (1989). Origin of the cusp Birkeland currents. *Geophysical Research Letters*, 16(2), 151–154. <https://doi.org/10.1029/GL016i002p00151>
- Saunders, M. A., Freeman, M. P., Southwood, D. J., Cowley, S. W. H., Lockwood, M., Samson, J. C., et al. (1992). Dayside ionospheric convection changes in response to long-period interplanetary magnetic field oscillations: Determination of the ionospheric phase velocity. *Journal of Geophysical Research*, 97(A12), 19,373–19,380. <https://doi.org/10.1029/92JA01383>
- Sazykin, S. (2000). *Theoretical studies of penetration of magnetospheric electric fields to the ionosphere* (Ph.D. Thesis). UTAH STATE UNIVERSITY.
- Siami-Namini, S., & Namin, A. S. (2018). Forecasting economics and financial time series: ARIMA vs. LSTM. *CoRR*, abs/1803.06386.
- Snekvik, K., Stgaard, N., Tenfjord, P., Reistad, J. P., Laundal, K. M., Milan, S. E., & Haaland, S. E. (2017). Dayside and nightside magnetic field responses at 780 km altitude to dayside reconnection. *Journal of Geophysical Research: Space Physics*, 122, 1670–1689. <https://doi.org/10.1002/2016JA023177>
- Tapping, K. F. (2013). The 10.7 cm solar radio flux (f10.7). *Space Weather*, 11, 394–406. <https://doi.org/10.1002/swe.20064>
- Wang, J., Tang, J., Xu, Z., Wang, Y., Xue, G., Zhang, X., & Yang, D. (2017). Spatiotemporal modeling and prediction in cellular networks: A big data enabled deep learning approach. In *IEEE INFOCOM 2017-IEEE Conference on Computer Communications* (pp. 1–9). IEEE.
- Waters, C. L., Anderson, B. J., & Liou, K. (2001). Estimation of global field aligned currents using the Iridium system magnetometer data. *Geophysical Research Letters*, 28(11), 2165–2168. <https://doi.org/10.1029/2000GL012725>
- Weimer, D. R. (2001). Maps of ionospheric field-aligned currents as a function of the interplanetary magnetic field derived from dynamics explorer 2 data. *Journal of Geophysical Research*, 106(A7), 12,889–12,902. <https://doi.org/10.1029/2000JA000295>
- Weimer, D. R., Ober, D. M., Maynard, N. C., Collier, M. R., McComas, D. J., Ness, N. F., et al. (2003). Predicting interplanetary magnetic field (IMF) propagation delay times using the minimum variance technique. *Journal of Geophysical Research*, 108, 1026. <https://doi.org/10.1029/2002JA009405>
- Wing, S., Sibeck, D. G., Wiltberger, M., & Singer, H. (2002). Geosynchronous magnetic field temporal response to solar wind and IMF variations. *Journal of Geophysical Research*, 107(A8), SMP 32–1–SMP 32–10.
- Wolf, R. A., Spiro, R. W., Sazykin, S., & Toffoletto, F. R. (2007). How the Earth's inner magnetosphere works: An evolving picture. *Journal of Atmospheric and Solar-Terrestrial Physics*, 69(3), 288–302. Global Aspects of Magnetosphere-Ionosphere Coupling.
- Zhang, C., Bengio, S., Hardt, M., Recht, B., & Vinyals, O. (2016). Understanding deep learning requires rethinking generalization. *arXiv preprint arXiv:1611.03530*.
- Zmuda, A. J., Martin, J. H., & Heuring, F. T. (1966). Transverse magnetic disturbances at 1100 kilometers in the auroral region. *Journal of Geophysical Research*, 71(21), 5033–5045. <https://doi.org/10.1029/JZ071i021p05033>